Precambrian Research 380 (2022) 106799

Contents lists available at ScienceDirect

Precambrian Research

journal homepage: www.elsevier.com/locate/precamres

Investigating the behavior of mid-Archean tides and potential implications for biogeochemical cycling

Eliana B. Crawford [a,b,c,*], Brian K. Arbic [a], Nathan D. Sheldon [a], Joseph K. Ansong [a,d], Patrick G. Timko [a]

[a] Department of Earth and Environmental Sciences, University of Michigan, Ann Arbor, MI 48109, USA
[b] Swift Navigation, 201 Mission St., Suite 2400, San Francisco, CA 94105, USA
[c] Department of Physics, Kenyon College, Gambier, OH 43022, USA
[d] Department of Mathematics, University of Ghana, Accra, Ghana

ARTICLE INFO

Keywords:
Archean
Banded iron formations
Continental shelves
Nutrients
Precambrian
Tides

ABSTRACT

A variety of different controls have been proposed for Precambrian marine productivity ranging from environmental factors such as temperature to the flux rate of nutrients (e.g., phosphorus) derived from the continents. In addition to other first-order differences in the Earth system such as a less luminous young Sun, the Earth and Moon were substantially closer together, which would have resulted in a greater tidal forcing. The potential biogeochemical implications of this enhanced forcing have been little explored. Here we use idealized bathymetries and continental configurations to examine mid-Archean ocean tides. We find that, even in the absence of realistic coastal geometries, mid-Archean tidal velocities, sea-surface height, and mixing equaled or exceeded modern values, and that there would have been higher frequency of extreme values. We use a modern tidal model with accurate coastal geometry (HYbrid Coordinate Ocean Model; HYCOM) to scale the idealized results. We propose that mid-Archean water parcel velocities would have been at least 4.5 times greater than at present, that sea-surface height would have been at least 2.5 times greater than at present, and that tidal mixing fronts would have been more common. Each of these factors would result in greater flux and distribution of nutrients, both due to exposure of the sea beds/nascent continents and enhanced onshore-offshore transport, potentially strongly influencing marine productivity even in the absence of substantial permanently exposed subaerial continental landmass.

1. Introduction

In the modern ocean, a substantial proportion of the total biological productivity takes place in the relatively shallow waters of the continental shelf (Walsh, 1991; Muller-Karger et al., 2005; Moore et al., 2013), with some areas acting as net carbon sources to the atmosphere and others as net carbon sinks from the atmosphere (e.g., Chen and Borges, 2009). Productivity is high both in tropical areas characterized by high temperatures (e.g., Behrenfeld et al., 2006) and also at cooler, higher latitudes in bathymetrically complicated areas like fjords (Smith et al., 2015). While either nitrogen or phosphorus may be limiting to marine productivity (e.g., Howarth, 1988; Tyrrell, 1999, Moore et al., 2013), most work on Precambrian primary productivity has focused on the role of phosphorus because while fixed nitrogen may be produced directly in the water column by diazotrophs, phosphorus is primarily delivered to marine ecosystems via transport of sediments derived from continental weathering (Bjerrum and Canfield, 2002; Planavsky et al., 2010; Jones et al., 2015; Reinhard et al., 2017; Lenton and Daines, 2017, 2018), and there is evidence for nitrogen fixation back to at least 3.2 Ga ago (Stüeken et al., 2015). This dependence on a continental phosphorus source in turn has implications for both water column and atmospheric oxygen levels because a nutrient-limited phototrophic biosphere would produce less net oxygen (e.g., Dzombak and Sheldon, 2020).

One relatively unexplored factor in this potential Precambrian nutrient limitation and in the balance between carbon sources and sinks is the role of tides. Tidal velocities have been shown to have a direct

Abbreviations: HYCOM, HYbrid Coordinate Ocean Model; MOM6, Modular Ocean Model version 6; SAL, self-attraction and loading; SSH, sea surface height.

* Corresponding author at: 776 Bush St., Apt. 402, San Francisco, CA 94108, USA.
E-mail addresses: crawforde@kenyon.edu (E.B. Crawford), arbic@umich.edu (B.K. Arbic), nsheldon@umich.edu (N.D. Sheldon), jkansong@umich.edu (J.K. Ansong), ptimko@umich.edu (P.G. Timko).

https://doi.org/10.1016/j.precamres.2022.106799
Received 8 March 2022; Received in revised form 17 June 2022; Accepted 15 July 2022

impact on the rate of sediment transport and deposition (Van de Kreeke and Robaczewska, 1993). Furthermore, in shelf regions with strong tides, mixing fronts develop (Simpson and Hunter, 1974), driving nutrient delivery that is critical to marine life. Tidal amplitudes also produce net effects on seabed irradiation and the spectral distribution of light over time, impacting photosynthesis and other photochemical processes in shallow water ecosystems (Bowers and Brubaker, 2010). Both the delivery and distribution of nutrients and the potential for changes to seabed irradiation could impact a variety of types of Precambrian sedimentation, including the deposition of chemical sediments like Lake Superior-Type banded iron formations (BIFS) that are only present in the Precambrian sedimentary record (e.g., Kappler et al., 2005; Posth et al., 2011), and which were particularly common during the Archean. In particular, questions remain about what the primary iron mineral phases are (e.g. Johnson et al., 2018 versus Robbins et al., 2019), how and in what form iron is transported from deep-sea hydrothermal vents onto continental shelf areas (e.g., Posth et al., 2013), and whether oxygen production in the water column through either photosynthesis or (indirectly) photoferrotrophy was a necessary condition for the formation of Superior-style BIFs (e.g., Konhauser 1998; Konhauser et al., 2002; Kappler et al., 2005; Konhauser et al., 2007; Bekker et al., 2010; Posth et al., 2014). Given that BIFs exhibit rhythmic bedding between iron-rich and iron-poor laminations, a variety of authors (Bontognali et al., 2013; Ojakangas, 1983; Ojakangas and Ojakangas, 2010; Walker and Zahnle, 1986; Watchorn, 1980) have proposed a tidal influence on their formation. However, a variety of critical parameters including the Earth's rotation rate (and hence length of day; e.g., Williams, 1997) and the total strength of the tidal forcing were substantially different during the Archean, making it problematic to use present-day observations to understand the role of Archean tides. Herein we explore the potential impacts of tides on nutrient and exposure dynamics on continental shelves in the Archean. We use a variety of idealized continental configurations and bathymetries to examine the sensitivity of tidal sea surface height (SSH) perturbations, tidal velocities, and the Simpson-Hunter parameter for tidal mixing fronts, to these poorly constrained environmental factors.

2. Background

2.1. Archean tidal forcing

Ocean tides represent a dynamical response to the equilibrium tidal forcing (Pugh, 1987; Cartwright, 1999). The lunar equilibrium forcing depends on Earth-Moon system parameters, including the Earth-Moon distance and the Earth's rotation rate. The Sun also causes tides, which are 46% as large as lunar tides for present-day conditions (Pugh, 1987; Cartwright, 1999); hence, solar tides are substantial, but smaller than the lunar tides. Lunar tidal forcing is proportional to the inverse of the cube of the Earth-Moon distance. Similarly, solar tidal forcing is proportional to the inverse of the cube of the Earth-Sun distance, which is substantially larger than the Earth-Moon distance. Tidal forcing contains a rich spectrum of tidal lines occurring at different periods, with clusters around one-half of Earth's rotation period (semidiurnal tides) and one Earth rotation period (diurnal tides). The dynamical response of ocean tides to tidal forcing depends upon several factors, including the Earth's rotation rate, frictional processes, the global configuration of continents and oceans, seafloor bathymetry, and solid-earth body and load tides (Hendershott, 1972; Pugh, 1987; Cartwright, 1999). Because of plate tectonic forces, the global basin geometry and seafloor bathymetry change over time (e.g., Condie, 1997). Therefore, although tides are predicted to a high degree of accuracy today, present-day tide models cannot provide information about the tides of the early Earth.

For a complete picture of mid-Archean tides, one must account for the unique astronomy, basin geometry, and bathymetry of the era. Tidal friction slows down the Earth's rotation rate (Munk and MacDonald, 1960; Lambeck, 1980; Williams and Boggs, 2016), implying that the Precambrian day length would have been shorter than it is today. Conservation of the total angular momentum of the Earth-Moon system then implies that the Earth-Moon distance must increase over time. The present-day increase in the Earth-Moon distance has been measured by lunar laser ranging to be 3.83 cm yr^{-1} (Williams et al., 1978; Dickey et al., 1994; Williams and Boggs, 2016). While exact values for Earth's rotation rate and the Earth-Moon distance during the mid-Archean are, of course, not available, plausible values can be estimated from models of the Earth-Moon evolution. For 3 Ga, studies place the Earth's rotation period at about 16 h and the Earth-Moon orbital radius at about 52 Earth radii (Ross and Schubert, 1989; Bartlett and Stevenson, 2016; Daher et al., 2021). See Table 1 for a summary of the differences between present-day and mid-Archean values of the Earth-Moon distance and rotation period. For simplicity, the forcing period of the mid-Archean principal lunar semidiurnal tide M_2 is assumed to be 8 h. Thus, the forcing frequency is computed as 2π / (8 h). The mid-Archean forcing amplitude of M_2 is determined from the present-day value scaled by the increase in the inverse of the cube of the Earth-Moon distance. For simplicity, the effects of changing Earth's obliquity, lunar orbit inclination, and lunar orbit eccentricity (e.g., Daher et al., 2021) on the M_2 forcing amplitude have been ignored here.

The effects of continental geometry and tidal forcing frequency on tides are associated with the concept of normal modes of oscillation and proximity to resonance. As with other oscillatory systems, the ocean has normal modes of vibration (Platzman, 1984, 1991; Müller, 2007, 2008, 2009). These normal modes are associated with both spatial patterns and frequencies, and are a function of seafloor depth (which controls the speed of shallow water gravity waves), the basin geometry (which sets the amount of time it takes for shallow water waves to propagate across basins), and other factors such as friction and the Earth's rotation rate. Large tides occur when the spatial patterns and frequencies of the normal modes have some degree of correspondence with the spatial patterns and frequencies of the tidal astronomical forcing. A close correspondence of the normal mode and forcing frequencies describes a resonant condition.

2.2. Archean continents and bathymetry

While regional bathymetries have been reconstructed for parts of the Precambrian (e.g., Pratt, 2001), because of plate tectonics, well-constrained whole-ocean bathymetries are not available for the Archean. It is generally assumed that early Earth's interior was much warmer and has since cooled through time (e.g., Holder et al., 2019) due to a combination of radioactive decay and direct heat loss at the surface. Crustal composition was generally more mafic and consisted of denser rock types (Lipp et al., 2021). Potential consequences of this are minimal surface topography (e.g., Rey and Coltice, 2008) and substantially less total emergent land until the Neoarchean (Flament et al., 2008), and deep ocean basins composed of denser rock types than in the Phanerozoic (Herzberg et al., 2010).

While there is significant ongoing debate about the timing of the onset of modern-style plate tectonics, most estimates range between 3.2 and 2.5 Ga (e.g., reviewed in Cawood et al., 2018). However, whether the onset of modern-style plate tectonics involved a proto-supercontinent (e.g., Capitanio et al., 2019) or numerous, smaller

Table 1
Present-day vs. mid-Archean M_2 tidal forcing.

Time period	Rotation period	Forcing frequency	Moon distance	Forcing amplitude
	hrs	$s^{-1} \times 10^{-4}$	Earth radii	m
Present-day	24	1.405	60	0.242334
Mid-Archean	16	2.182	52	0.372270

more widely spaced micro-continents remains an open question. Thus, without a single strongly supported Archean bathymetry, we instead consider this as an opportunity for a sensitivity test of different potential surface configurations of both emergent land and continental shelf width, and use a modern depth structure (see *3.1*) as in previous attempts to model Archean oceanic biogeochemistry (e.g., Olson et al., 2013).

3. Simulation details

3.1. Bathymetries

Researchers have taken a variety of approaches to modeling prehistoric oceans in eras with uncertain bathymetries. One climate model of the late Mesoproterozoic era was conducted with a single bathymetry model construction for 1.0 Ga and several simulations with different continental rotations (Fiorella and Sheldon, 2017). Green and Huber (2013) employed a paleo-reconstruction of the 55 Ma geometry to simulate tides in the early Eocene, while Green et al. (2017) employed paleo-reconstructions of several epochs to model deep-time tides. Another recent study employed three paleobathymetry reconstructions (at 55 Ma, 116 Ma, and 252 Ma), as well as a present day bathymetry, randomly shuffled to roughly simulate plate tectonic motions throughout the Earth's history (Daher et al., 2021). A randomized fractal approach was employed by Blackledge et al. (2020) to generate a variety of continental configurations for simulations of past, present, and future ocean tides.

Because no realistic depth profile maps exist for the mid-Archean era, we adopt an approach that is somewhat similar to that used by Blackledge et al. (2020) in that the continents are generated from first principles. The landmasses in our study are systematically designed, and are more idealized than the fractal geometries in Blackledge et al. (2020). We design several idealized bathymetries with simplified block geometries because they are easy to construct and manipulate. Our objective with these geometries is to gauge the effects of various bathymetrical features on the tides by changing some continental characteristics while holding others constant. None of the simulation results obtained using these maps are assumed to be quantitatively representative of the mid-Archean period, although we can predict that some are likely to be more realistic than others. The geometries are designed to build a qualitative picture of how mid-Archean tides would have compared to present-day tides under various assumptions. The bathymetries used here specifically allow us to assess the tidal response to halving the total land area, doubling the continental shelf area, decreasing the average depth of the ocean, and changing the size, number, and position of the continents.

The present-day Earth geometry and bathymetry (Smith and Sandwell, 1997) is used as a reference point for all idealized maps developed in this study. The present-day geometry/bathymetry is designated as bathymetry 0 in Table 2 and is depicted in Fig. 1 on a latitude-longitude coordinate system, clipped at 82°S and 82°N. This trimming near the poles—accomplished by means of artificial walls—is required for all bathymetries in this study because grid cells become very small at these latitudes, thus necessitating small time steps and slowing down the model. All comparative bathymetry statistics shown in Table 2 are computed for clipped bathymetries.

An idealized version of the present-day Earth continental geometry and bathymetry has been developed for use as a control (Fig. 2a). It has two large block continents separated by oceans of different sizes—one twice as wide as the other. The configuration represents the Americas and Afro-Eurasia, with the Atlantic and Pacific oceans between them. The water volume and average depth of the ocean, as well as the proportional areas of land, continental shelf, and deep-ocean, are matched as closely as possible to those of the present-day Earth. For real continental edges today, the shelf-slope break depth varies between ~20 and 500 m (Fairbridge and Bourgeois, 1978), but is generally fairly consistent and often at or near the photic zone (Emery and Uchupi, 1984). We represent simple continental shelves and slopes in the idealized bathymetries by overlapping two logistic curves. The shelf cut-off depth (the limit of the first logistic curve) is set to 135 m, which is the average break depth of present-day shelves (Heezen et al., 1959).

Starting with the simplified control, or "Default" bathymetry (Fig. 2a), we create the other geometries used in the simulations by systematically altering proportions of land and shelf, ocean floor depth,

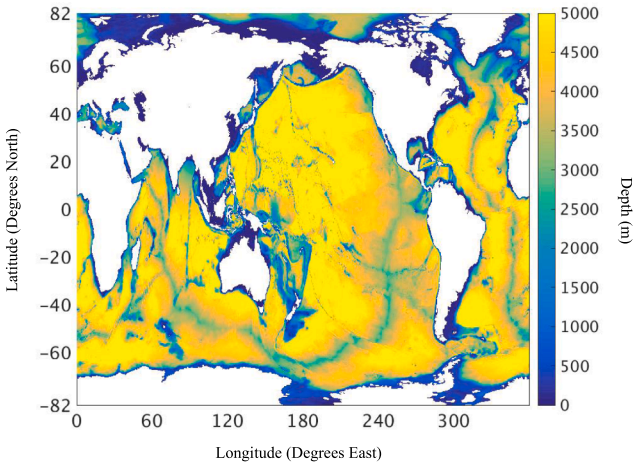

Fig. 1. Bathymetry 0 – Present-Day Bathymetry ("Real"). **Description:** In order to properly render shelves and shallow seas, the color scale saturates at 5,000 m. The maximum depth in the bathymetry is 9822 m.

Table 2
Summary statistics for idealized bathymetries.

ID	Name	Classification	Max Depth	Mean Depth	Water Volume	Land	Shelf	Intermediate Depth	Deep Ocean
			m	*m*	$10^{18}\ m^3$	%	%	%	%
0	Real	(Reference)	9822	3684	1.328	**28.7**	**4.1**	5.7	61.5
1	Default	Control	4285	3684	1.327	**28.7**	**4.2**	5.5	61.6
2	Half Area Deep	Transitional	4285	3790	1.641	14.3	**4.2**	5.4	76.0
3	Half Area	Transitional	4164	3683	1.595	14.3	**4.2**	5.4	76.0
4	Twice Shelf	Mid-Archean	4164	3487	1.510	14.3	8.4	5.4	71.9
5	Translated Lon.	Mid-Archean	4164	3487	1.510	14.3	8.4	5.4	71.9
6	Translated Lat.	Mid-Archean	4164	3486	1.510	14.3	8.5	5.4	71.8
7	Broken	Mid-Archean	4244	3488	1.510	14.3	8.4	5.3	72.0
8	Supercontinent	Mid-Archean	4179	3488	1.510	14.3	8.4	5.3	72.0

Description: All percentages in this table represent area-weighted percentages of total grid cells. For example, the 'percentage of land' represents the total percentage of area in the bathymetry that would be considered land. Land is defined as having depth $\leq$ 0 m. Continental shelves are regions with 0 m $<$ depth $\leq$ 135 m. Intermediate depths are those with 135 m $<$ depth $\leq$ 1500 m. Deep ocean constitutes all remaining area with depth $>$ 1500 m. (For bathymetries that are not considered to be representative of the Mid-Archean, the characteristics that specifically disqualify them are shown in bold).

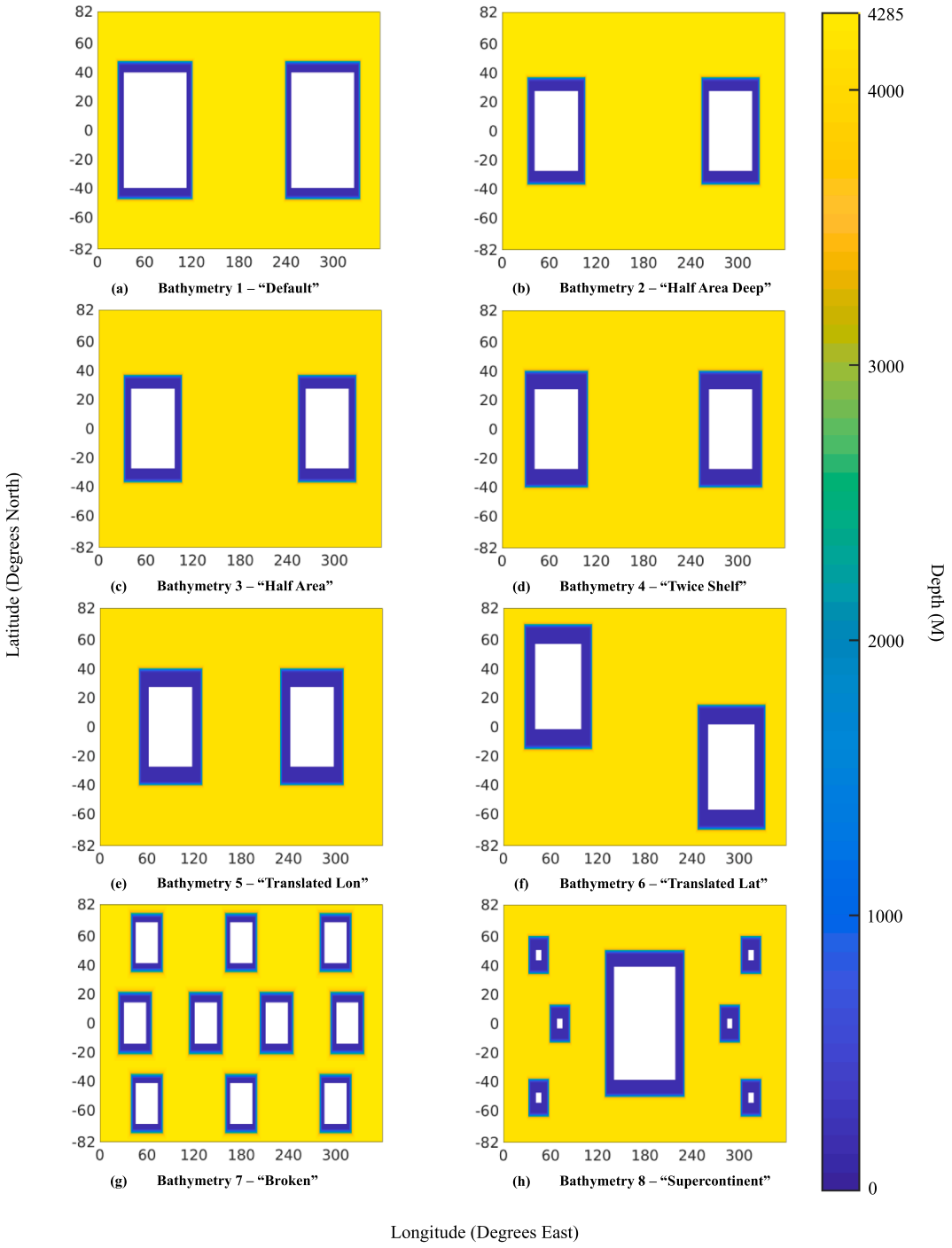

Fig. 2. Idealized bathymetries. **Description**: Bathymetries are clipped at 82°N and 82°S for computational purposes. See Table 2 for descriptions of (a)-(h).

and continental placement. All of the idealized bathymetries are depicted in Fig. 2. The second bathymetry (Fig. 2b) is constructed from the control by cutting the land area roughly in half. Because decreasing the proportion of land increases the average depth, an additional bathymetry (Fig. 2c) is subsequently made by raising the deep-ocean floor level to negate this change. From there, we make another map by doubling the continental shelf size (Fig. 2d). In all other geometries created after this point (Fig. 2d-h), we hold the depth profile roughly constant and alter the continental configurations. It should be noted that "a roughly constant depth profile" in this case means holding the percentages of land, shelf, slope (or regions of "intermediate depth"), and deep ocean roughly constant, while modifying the maximum depth–and thus, the water volume—to achieve this purpose. We made this decision with the hypothesis that small modifications to the water volume and maximum depth of the ocean would have less of an impact on the tides (particularly those in the continental shelf regions) than the amounts of land area and shelf area. The validity of this assumption is investigated in Section 4.6 based on results from simulations using transitional bathymetries 3 and 4.

Of the maps with modified continental configurations, one (Fig. 2e) examines the effect of shifting the longitudinal positions of the continents relative to each other, or in other words, widening the "Atlantic-like" ocean and narrowing the "Pacific-like" ocean. Another (Fig. 2f) tests the effect of latitudinal translation of the continents, or moving the

continents so that their northern and southern boundaries no longer coincide and more continental landmass is placed at extreme latitudes up to 70°N and 70°S. In another bathymetry (Fig. 2g), the total land area is broken up into many smaller continents to simulate the postulated early stages of plate tectonics prior to the aggregation of large continental landmasses, sometimes termed a "micro-continent" or "island-arc" world. A final geometry (Fig. 2h) represents a super-continent model, in which the majority of the land area is combined into one large continent, with the remainder placed in several smaller islands, which could be considered analogous to island-arc settings. Comparative statistics for each of the eight idealized maps, and for real present-day bathymetry, are summarized in Table 2.

In Section 2.1, we discussed the hypothesized geometrical differences between the mid-Archean and present-day bathymetries. Two primary characteristics that we choose to focus on in this study are the differences in land area and shelf size. Therefore, all of the bathymetries are categorized based on these two characteristics: all maps with roughly half the land area and twice the shelf area of the control are classified as "Mid-Archean", while remaining maps are termed "Transitional". Transitional maps, while not the primary focus of this work, are used to create potentially useful simulations that isolate the effects of one astronomical or bathymetrical characteristic on tidal processes.

There are known limitations to working with idealized geometries. Due to the uniformity and simplicity of the coastline, the bathymetries used in this study lack the intricate bays and other shallow water features typically associated with large resonant tides in the continental shelves (e.g., Pugh, 1987; Egbert and Ray, 2000; Arbic et al., 2007, 2009, amongst many). It should be noted that more intricate coastal features such as the Bay of Fundy, where tides are particularly high, are not well resolved at the grid resolution we are using. In light of these limitations, we expect that the results produced by our simulations represent a realistic lower bound for Precambrian shelf tides, but they cannot be extended to predict extreme high shelf tides quantitatively. Shoreline complexity is a function of many processes, with glacial history being a key control. The oldest currently documented glaciation is the ~2.9 Ga ago Pongola Glaciation (e.g., Eriksson et al., 1998; Young et al., 1998; Luskin et al., 2019), so there is no reason to expect shoreline complexity at the time simulated herein was different than today. Therefore, we can still consider the frequency of and relative differences between extreme tides across the simulations to be qualitatively informative, but note that this relationship may not be true for earlier parts of the Archean or the Hadean.

3.2. Tide model

The governing equations for tides can be found in many sources including Hendershott (1972), Pugh (1987), Arbic et al. (2004), and references therein. The Modular Ocean Model version 6 (MOM6), taken from Hallberg, 2015, is used in one-layer (barotropic) shallow-water mode to time-evolve the tidal equations for sea surface height (SSH) and parcel velocity ($\vec{u}$) on the model bathymetries described above. To simplify the study, we only simulate the principal lunar semidiurnal tide (M_2), which is the largest tidal constituent in the ocean and which by itself accounts for about two thirds of the present-day tidal energy dissipation (Egbert and Ray, 2003). Modeling additional tidal constituents, such as S_2 and K_1, would involve additional computer resources and analysis time. Due to the exploratory nature of this study, we decided that this would be best left to future work.

As in almost all modern tide simulations, the simulations we performed for this paper include a quadratic bottom boundary layer drag, which dissipates energy primarily in shallow regions where tidal velocities are large (e.g., Arbic et al., 2004; Egbert et al., 2004; Egbert and Ray, 2000, 2003; Jayne and St Laurent, 2001). Many modern tide models also include a parameterized topographic internal wave drag, which accounts for the generation and ultimate breaking of internal waves generated by tidal flows over topographic features (e.g., Arbic et al., 2004; Egbert et al., 2004; Egbert and Ray, 2000, 2003; Jayne and St Laurent, 2001). Wave drag depends not only on topography but also on stratification. Therefore, wave drag terms vary spatially in complex patterns. For simplicity, in the present paper we used a spatially constant linear wave drag scheme, rather than a spatially varying wave drag. We do this in part because our bathymetries do not include topographic features in the deep ocean. We conduct several simulations with present day astronomical conditions using bathymetry number 1 (the "default" bathymetry) to tune the drag coefficient. The linear drag value resulting in tidal energy dissipation closest to the present-day M_2 dissipation value of 2.4 TW (Egbert and Ray, 2003) after two iterations of the self-attraction and loading term (SAL, see below) is then selected and used for all subsequent simulations. Because ocean stratification varies over deep time, and because wave drag depends on stratification, deep-time tidal dissipation will depend on stratification. Sensitivities to assumed ocean stratification values are left as a topic for future work. For now, we note that Green et al. (2017) found that the sensitivity of tide simulations to changes in wave drag (motivated by likely changes in stratification) is actually fairly small.

With input parameters established, each of the simulations is run through four iterations of the SAL term (Hendershott, 1972; Ray, 1998). The SAL term accounts for self-attraction (self-gravitation) of the tides upon themselves, for the deformation of the solid earth due to tidal loading, and for the self-attraction of the tidal load-deformed solid earth. The term is computed by decomposing the tidal elevations into spherical harmonics, and taking an inverse spherical harmonic transform after accounting for the different loading effects for each degree of harmonic. Because this is computationally expensive, an iterative procedure is often used (e.g., Arbic et al., 2004, amongst others). A scalar approximation (Ray, 1998), equal to the tidal elevation perturbation multiplied by a coefficient with a value of about 0.1 for present-day conditions, is often taken as a simplification for the SAL term. Here, because the very different mid-Archean conditions are likely to yield a different optimal SAL scalar coefficient, we first determine the coefficient values. For each of the bathymetries in Table 2, we conduct a "run 0" with no SAL term. After run 0 is completed, we perform a least-squares fit on the SAL terms, computed offline using the full spherical harmonic treatment, against the tidal elevations themselves. The slope of the least-squares fit provides a scalar SAL coefficient (ß) that we use in a first scalar

Table 3
Summary of simulations and their inputs.

ID	Bathymetry ID / Name	Forcing frequency	Forcing amplitude	Classification	ß
1	**1 - Default**	**Present-day**	**Present-day**	Control	0.1202
2	**1 - Default**	Mid-Archean	Mid-Archean	Transitional	0.0955
3	**2 – Half Area Deep**	Mid-Archean	Mid-Archean	Transitional	0.1124
4	**3 – Half Area**	Mid-Archean	Mid-Archean	Transitional	0.1122
5	4 – Twice Shelf	Mid-Archean	Mid-Archean	Mid-Archean	0.1017
6	4 – Twice Shelf	Mid-Archean	**Present-day**	Transitional	0.1014
7	5 – Translated Lon.	Mid-Archean	Mid-Archean	Mid-Archean	0.1063
8	6 – Translated Lat.	Mid-Archean	Mid-Archean	Mid-Archean	0.1039
9	7 – Broken	Mid-Archean	Mid-Archean	Mid-Archean	0.0934
10	8 – Supercontinent	Mid-Archean	Mid-Archean	Mid-Archean	0.0948

Description: For simulations that are not considered to be representative of the Mid-Archean, the characteristics that specifically disqualify them are shown in bold.

approximation of the SAL term (Ray, 1998). Values of ß that were calculated for each simulation are included in Section 2.3, Table 3. This scalar coefficient is then used in "run 1". After run 1 is completed, the SAL terms are again computed offline with spherical harmonics, and the results of run 1, in the form of tidal amplitude and phase maps, are used in "run 2". An identical process is used to initiate "run 3" from "run 2" output data, and the results of this study are based upon analysis of "run 3" for each geometry. Arbic et al. (2004) found that three iterations of the SAL term are generally sufficient to achieve near-convergence. The computed total power dissipation can be used to check the convergence of the model. For our simulations, the power output varied by 15% or less between the second and third iterations.

In the simulations, each iteration runs for 56 model days. To verify that the system has reached a steady state, we examine plots of kinetic and potential energy over time. The simplified techniques employed to solve for the tidal amplitudes and phases require the data analyzed to represent an integer number of full lunar days. Therefore, in each simulation, the number of model hours used in analysis is chosen based on the Earth's rotation rate. For simulations with present day rotation rates, 25 h is chosen, as it is actually closer to the exact lunar day length (twice the period of M_2) than 24 h. For Mid-Archean simulations with a 16-hour rotation period, 16 h of data are used for tidal analysis.

3.3. Simulation design

In total, 10 different ocean tide simulations were conducted in this study, and the input parameters are summarized in Table 3. The control, or "Default", uses present-day astronomical conditions and the default (control) bathymetry. The remaining simulations are divided into two categories. Just as bathymetries are classified as "Mid-Archean" or "Transitional" in Table 2, simulations are also deemed as representative of the Mid-Archean period or not. For a simulation to qualify as "Mid-Archean", it must use a bathymetry that is classified as Mid-Archean, as well as the Mid-Archean values for tidal forcing and frequency discussed in Section 2.1. Any simulations lacking one or more of these requirements are considered "Transitional"; they are helpful in assessing the importance of various bathymetrical and astronomical characteristics with regard to the tides, but they are not considered to represent tides during the Mid-Archean period for the purposes of this study. With a few exceptions, data output from transitional simulations 2, 3, 4, and 6 will not be included in the main body of the paper but will be available as supplemental material.

Table 4
Total power dissipation for each simulation.

ID	Bathymetry ID / Name	Forcing frequency	Forcing amplitude	Classification	Power dissipation TW
1	1 – Default	Present-day	Present-day	Control	2.352
2	1 – Default	Mid-Archean	Mid-Archean	Transitional	2.077
3	2 – Half Area Deep	Mid-Archean	Mid-Archean	Transitional	6.077
4	3 – Half Area	Mid-Archean	Mid-Archean	Transitional	5.495
5	4 – Twice Shelf	Mid-Archean	Mid-Archean	Mid-Archean	5.576
6	4 – Twice Shelf	Mid-Archean	Present-day	Transitional	2.544
7	5 – Translated Lon.	Mid-Archean	Mid-Archean	Mid-Archean	4.575
8	6 – Translated Lat.	Mid-Archean	Mid-Archean	Mid-Archean	3.491
9	7 – Broken	Mid-Archean	Mid-Archean	Mid-Archean	3.915
10	8 – Supercontinent	Mid-Archean	Mid-Archean	Mid-Archean	2.729

Description: Simulation characteristics are repeated here for convenience.

4. Results & discussion

4.1. Power dissipation

The tidal power dissipation values in the simulations are listed in Table 4. For all ten simulations shown, the power dissipation matches the power input to within 1.2% or less. Comparison of simulations 5 and 6 verifies that total dissipation drops with increased moon distance if all other factors are held constant, and the decrease is roughly proportional to the squared ratio of the tidal forcing amplitudes[1], as expected. However, we observe a drop in the power dissipation from simulation 1 to simulation 2, despite the decrease in Earth-Moon distance. This indicates that changes in the favorability of resonance conditions, due to the Earth's rotation rate and continental geometry (e.g., Webb, 1982; Bills and Ray, 1999; Daher et al., 2021), can cancel the effects of lunar proximity. The results of simulation 1 suggest strong resonance matching between the present-day idealized continental geometry and the present-day tidal forcing frequency. Those resonance conditions break down in simulation 2 for the same bathymetry with Precambrian tidal forcing (higher frequency). Results from the mid-Archean simulations, however, suggest more favorable resonance matching conditions than the control. All of the mid-Archean simulations with two or more large continents show an energy dissipation gain of over 1 TW. The supercontinent model stands out with the smallest dissipation gain ($<$0.5TW). Despite the wide range in the power dissipation values across the mid-Archean simulations (standard deviation of 1.1TW), each is at least 16% greater than the control. Averaging these yields a power dissipation of 4.1 $\pm$ 0.5 TW, a statistically significant increase over the present day.

4.2. Global SSH maps

Global maps of SSH amplitude can be useful for the insight they provide concerning resonance conditions and total power dissipation. Side-by-side comparisons of similar simulations are particularly insightful for this purpose. Fig. 3 shows a comparison of SSH amplitudes for simulations 1 and 2, as well as 5 and 7. The control geometry is used in the first two, but the Earth-Moon radii and tidal forcing periods differ. Recall that despite the increased lunar proximity in simulation 2, the tidal power output drops (Table 4). Therefore, the control bathymetry is not as resonant under Precambrian astronomical conditions. The breakdown of resonance between simulations 1 and 2 is clearly reflected in the figure. In the first simulation (Fig. 3a), large regions of high amplitude exist along the equator between the two continents. Conversely, in simulation 2 (Fig. 3b), the total area with high SSH amplitudes appears to be smaller, and we see smaller amplitude extremes, indicative of weaker tidal resonances.

A similar comparison can be performed for simulations 5 and 7, which are identical except for the longitudinal positions of the continents. Simulation 7 (Fig. 3d) has continents that are shifted closer together by 41.625° longitude, effectively shrinking the Pacific Ocean. Differences in resonance matching are readily apparent between the two models. Simulation 5 displays a larger number of high-amplitude regions and dissipates over 1 TW more energy than simulation 7. In both simulations, however, the power output is higher than in the control (Table 3); both simulations have higher average SSH amplitudes than the control simulation (Fig. 3a), especially at higher latitudes.

While global maps can provide big-picture information about the tides, the remainder of the discussion will focus on tidal statistics in the continental shelf regions ($\leq$135 m depth), as these are the regions with the largest proportion of primary productivity, and they are also where

[1] The drop is about 8% less than expected, and this discrepancy is likely due to nonlinearities in the model.

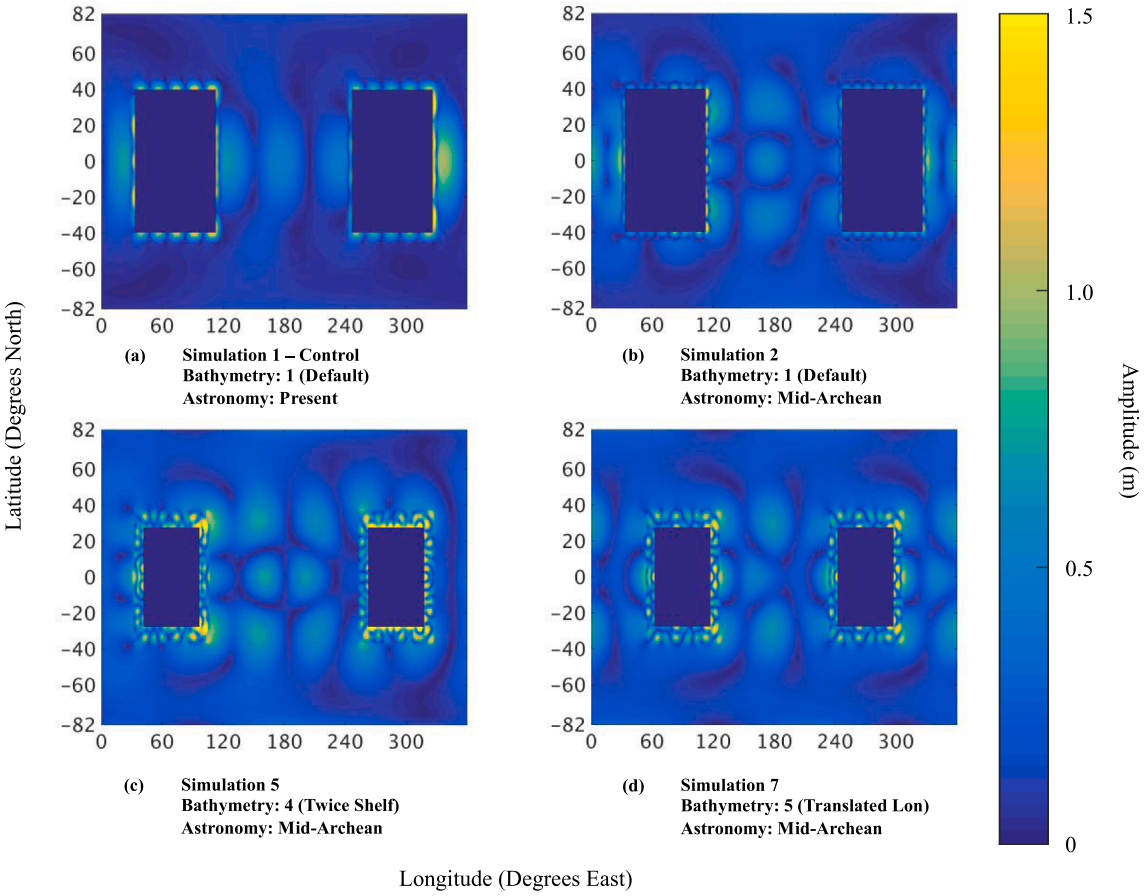

Fig. 3. Global SSH amplitude comparisons for select simulations.

geologically critical sediment types such as BIFs are most often deposited (Gross, 1980; Trendall, 2002; Bekker et al., 2010; Konhauser et al., 2017). Data for each result will be presented in histograms with log-scaled shelf area on the y-axis and the physical oceanographic parameter on the x-axis. Shelf areas are presented as percentages because the true amount of continental shelf area during the mid-Archean is poorly constrained and because the raw shelf area is not the same for all the bathymetries. For each parameter, histogram plots for the control and the five mid-Archean simulations will be shown. Histogram plots of each parameter for transitional simulations 2, 3, 4, and 6 are not in the text but are included as supplemental figures S1, S2, and S3.

In addition, data from a simulation (Timko et al., 2019) of a modern ocean tide model with realistic continents is introduced. The simulation was performed at 0.08° resolution with the HYbrid Coordinate Ocean Model (Chassignet et al., 2009) and is referred to here as simulation #11, or "HYCOM". MOM6 and HYCOM are comparable, and both are capable of simulating tides under idealized or realistic conditions. We chose to use output from a realistic simulation of HYCOM because the simulation had already been completed and was thus convenient to use. Here, we use results for the M_2 tidal component. In each section, a histogram from the HYCOM simulation is displayed next to the control histogram. Comparing output data from the HYCOM simulation against data from the idealized control allows us to hypothesize how mid-Archean tidal conditions in the presence of realistic coastlines may have differed from our idealized-geometry simulations. For the HYCOM bathymetry plot, refer to supplemental figures.

4.3. Sea surface height (SSH) in the continental shelves

In Fig. 4, SSH amplitudes for each of the mid-Archean simulations are compared to the control amplitudes. In the control, 1.4 m represents roughly the cutoff point for the top 95th percentile of SSH amplitudes. For each simulation, the percentage of shelf area with SSH amplitudes at or above this 'critical value' is calculated and displayed on the plot. A dashed line is drawn in each plot at the location of the critical value (fixed at 1.4 m) and a solid line is drawn at the mean value (variable).

Amongst the 5 representative mid-Archean simulations, the mean SSH amplitudes and the percentages of amplitudes above the critical value are comparable to the control, with some simulations achieving higher values and others lower depending on which continental geometry is used. Interestingly, all 5 of the representative mid-Archean simulations have more skew toward high values, achieving higher SSH extremes than the control, regardless of which bathymetry is used. In other words, SSH amplitudes in the mid-Archean simulations generally have higher extremes, and this trend holds even for simulations that do not have higher mean values, although the size of the maximum values remains bathymetry dependent.

The impact of resonance conditions on the summary statistics is readily apparent when comparing simulations 5 and 7, where the two continents have the same shapes and sizes in both geometries. The change in distance between the two continents alone from simulation 5 to 7 causes roughly a 16% drop in the weighted mean and a 51% drop in the percentage of shelf SSH values above the critical threshold. Recall from Table 4 that simulation 7 also has roughly an 18% drop in power dissipation as compared to simulation 5, indicating that simulation 7 has less favorable resonance conditions. Because the shapes of the coastlines, continental slopes, and ocean basins are identical in these two simulations, the difference in the SSH amplitudes must be attributed to resonance conditions, and not these other factors. Therefore, there is at least some positive correlation between favorable resonance conditions (as measured by power dissipation) and high SSH values.

Comparing simulations 7 and 9, we can see that the impact of

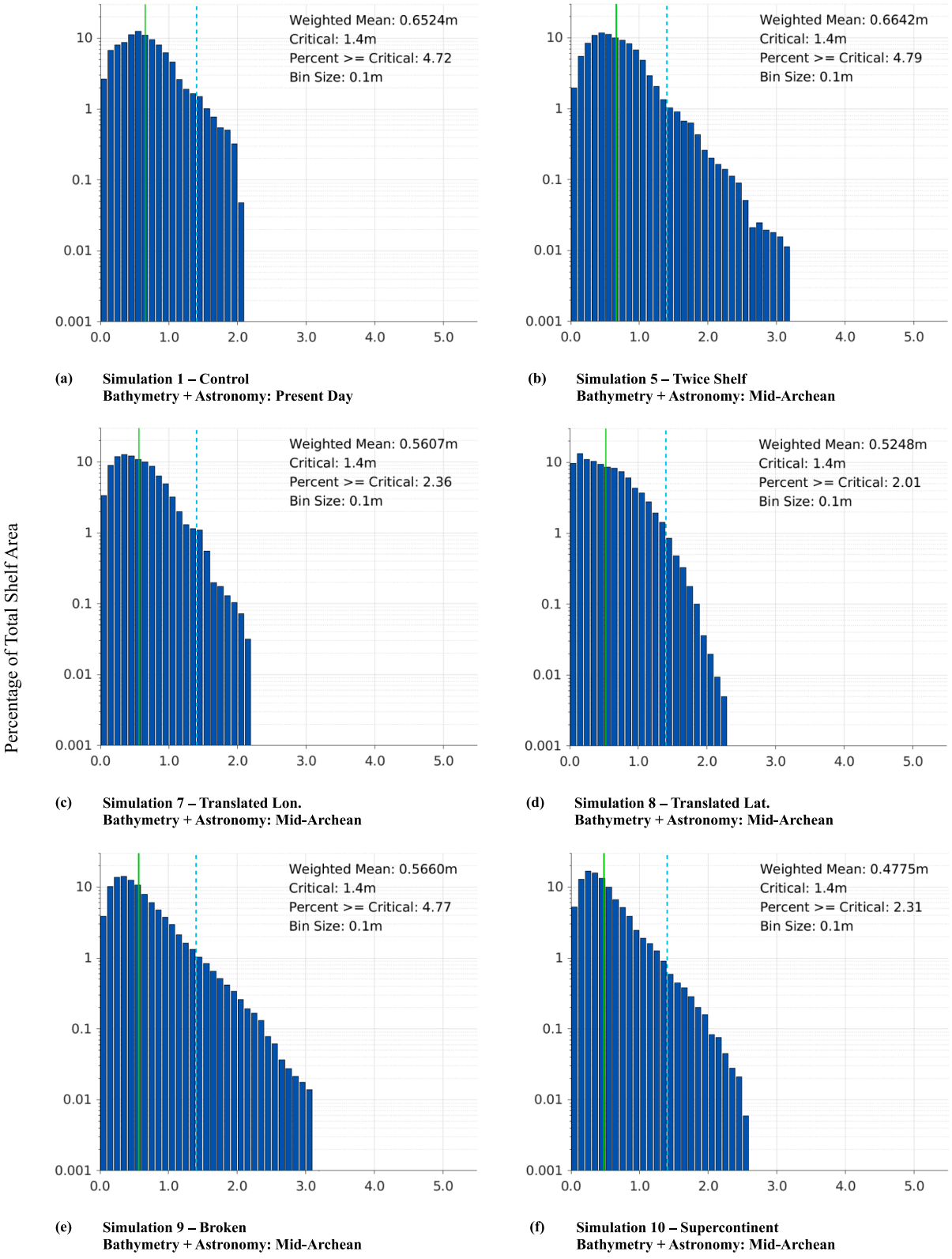

Fig. 4. SSH amplitudes in the continental shelves.

resonance conditions competes with other factors related to continental geometry. The tides in simulation 9 dissipate about 14% less power than simulation 7, but achieve almost the same weighted mean SSH amplitude (1% greater) and nearly double the percentage of SSH amplitudes above the critical value (102% greater).

To understand what these idealized simulations could imply for SSH amplitudes in the presence of realistic coastlines, we display a comparison of HYCOM shelf SSH values against the control (Fig. 5). It is readily apparent that the realistic bathymetry results in a lower mean SSH value and many more grid points with small SSH values (approaching zero). The idealized geometry seems to artificially reduce the number of SSH amplitudes in the 0 m–0.3 m range. Perhaps this is due to the fact that the lower grid resolution and the logistic curves used in this study result in too few grid cells with very shallow depths like those we might expect to see directly adjacent to coastlines. Most of the continental shelf points in the idealized geometries are much nearer to the 135 m shelf break depth. It is a reasonable assumption then that realistic mid-Archean geometry conditions would have also resulted in a much larger percentage of SSH amplitudes below 0.1 m than are seen in the idealized datasets (closer to 11%, as seen in the present day model).

Perhaps more interesting is the large difference between extreme SSH values in Fig. 5a and Fig. 5b. The realistic coastline results in an SSH extreme that is nearly 2.5x greater than we observe in the idealized control and a roughly 19% increase in the number of extreme values as well (5.63% vs. 4.72%). Given that information, it is reasonable to say that the extremes in plots 4b–4f are a lower bound for the SSH extremes we would expect to see in the mid-Archean. If the scale factor is also 2.5x, this means that SSH extremes would have easily surpassed 5 m, and may have even achieved 6 m. An increase in extreme tides relative to the modern distribution suggests that, in at least some parts of the world, more of the seabed was exposed episodically than under present conditions and with greater frequency because of the shorter day duration. As a result, greater nutrient delivery and recycling due to tidal processes would have been possible in such locations. More complex bathymetries with higher spatial resolution would be needed to assess this quantitatively.

4.4. Parcel velocity semi-major axis in the continental shelves

The parcel velocity is a vector with east–west and north–south components ($u(t)$ and $v(t)$, respectively, where t represents time). A phase diagram of the overall velocity appears as an ellipse, whose orientation and ratio of semi-major axis to semi-minor axis are dependent on the amplitudes and phases of $u(t)$ and $v(t)$, which we refer to as (U, g_u) and (V, g_v), respectively. Here, we focus on the semi-major axis *(A)*, which is interpreted as the maximum parcel speed achieved in one cycle of the tides and is given by the following equations (Pugh, 1987):

$$A = \sqrt{\frac{U^2 + V^2 + \alpha^2}{2}} \tag{1}$$

$$\alpha^2 = \sqrt{U^4 + V^4 + 2U^2V^2\cos 2(g_u - g_v)} \tag{2}$$

Histograms of A in the continental shelves are shown in Fig. 6. Vertical lines are drawn at 0.3 m s^{-1}, which is roughly the 96th percentile cutoff for the control simulation. For each simulation, the percentage of shelf area with A at or above this 'critical value' is calculated and displayed on the plot.

In contrast to the SSH results, all of the mid-Archean simulations achieve higher mean A values than the control, and all simulations but the supercontinent simulation achieve higher percentages of A values above the critical threshold. All but the translated longitude simulation achieve higher extreme velocity amplitudes than the control as well. Simulation 5, which has the highest global power dissipation, stands out with the highest mean and the highest percentage of values above the critical threshold. However, high global power dissipation does not appear to have as great an impact on the presence or size of extreme velocity amplitudes. The broken continent and supercontinent models stand out with the highest extreme velocities and the greatest number of extreme outliers, despite having global power dissipation values that are relatively low amongst the mid-Archean simulations.

Interestingly, the 0.8–0.9 m s^{-1} bin is empty for all of the simulations. For simulations achieving values higher than 0.9 m s^{-1}, there is actually a gap in the plot at the 0.8–0.9 m s^{-1} range. The reason for this is not clear. However it is worth noting that tidal velocities still achieve values in this range. Rather, the value of A (the maximum speed of the velocities in a particular area) never falls in the 0.8–0.9 m s^{-1} range.

Comparing the HYCOM simulation to the control (Fig. 7), we see that idealized continents result in much smaller extreme velocities than realistic ones. The highest value of A achieved by the HYCOM simulation is over 4.5x greater than that of the control. If we assume a similar scale factor for the mid-Archean, then realistic coastlines may have resulted in extreme velocities larger than 4 m s^{-1} for many continental configurations (note that simulation 7 stands out as the one mid-Archean simulation with a velocity extreme smaller than that of the control).

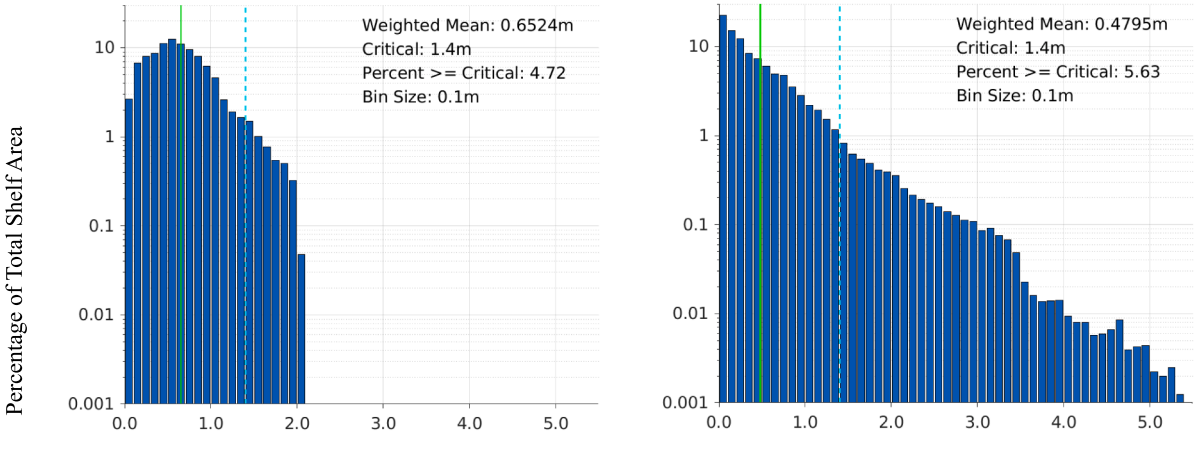

Fig. 5. SSH amplitudes in the continental shelves (control vs. HYCOM).

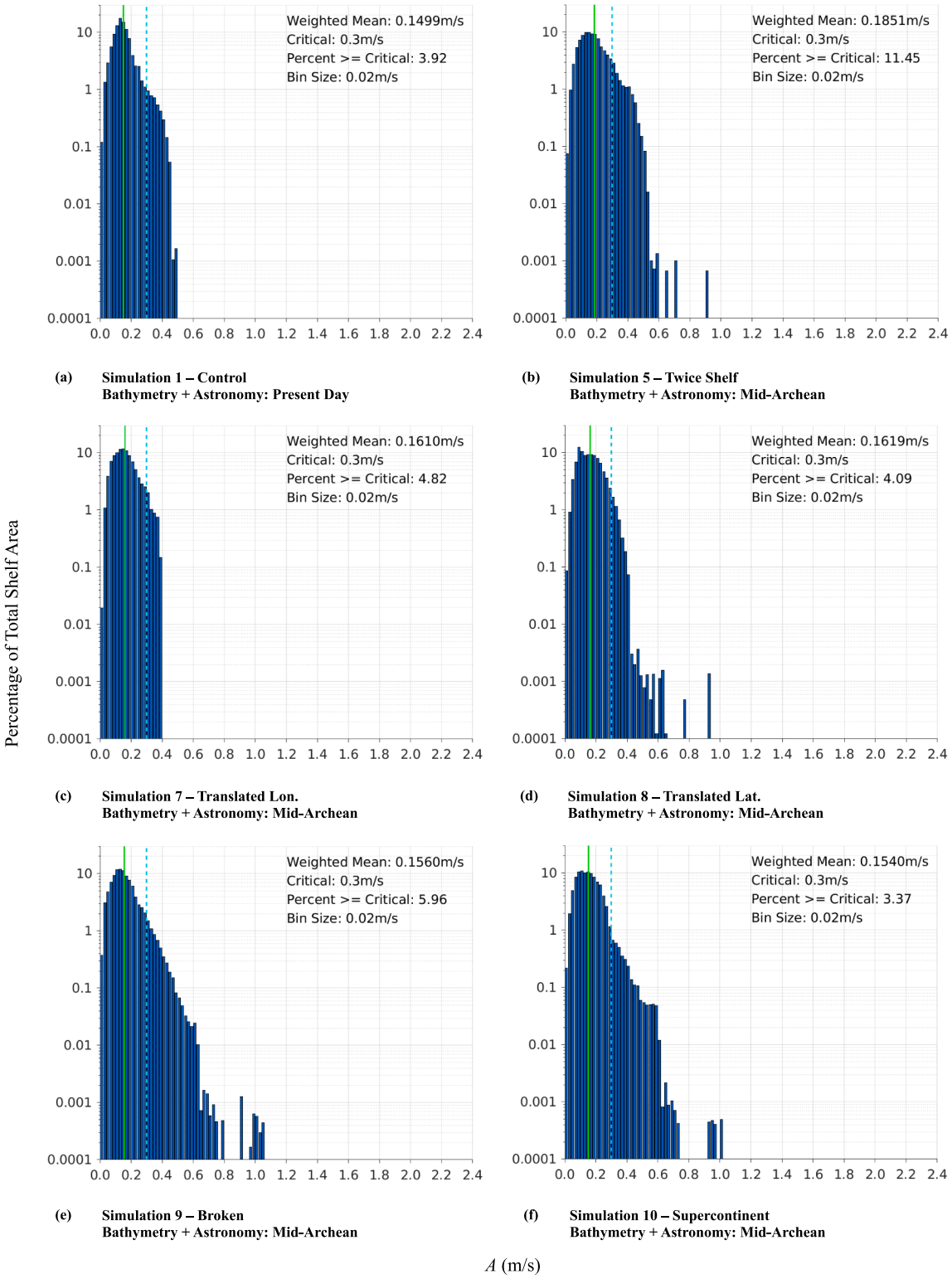

Fig. 6. Parcel velocity semi-major axis values *(A)* in the continental shelves.

To gain a sense for the geological significance of this increase in extreme velocities, we've aligned boxplots of the data with the Hjulström particle flow diagram (Earle, 2015) in Fig. 8. We see that the realistic HYCOM present day simulation does not achieve high enough tidal extremes to erode or transport particles larger than 100 mm. However, if the mid-Archean did experience tidal velocities as large as 4 m s^{-1} or more, as suggested, then that would be just fast enough to transport 1000 mm particles and to erode 100 mm particles. It has been shown that the composition of the weathering product on continents has not changed dramatically through time (Dzombak and Sheldon, 2022). However, the type of fluvial distribution of those sediments (braided versus meandering) and their relative grain size distributions have changed significantly, in particular with the rise of land plants in the Paleozoic (Gibling and Davies, 2012). Young (2019) notes that much of

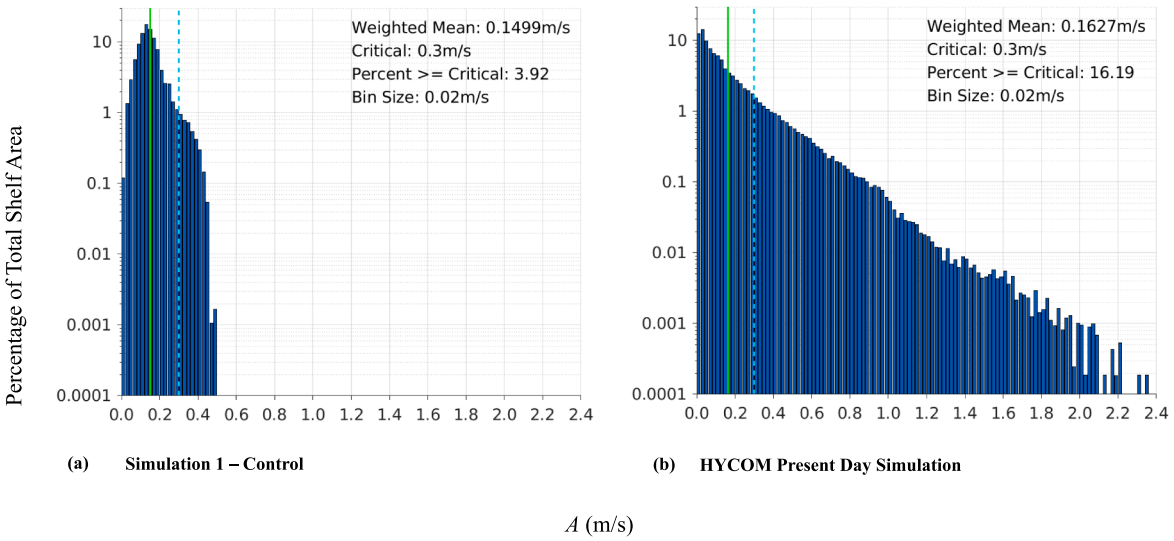

Fig. 7. Parcel velocity semi-major axis values *(A)* in the continental shelves (control vs. HYCOM).

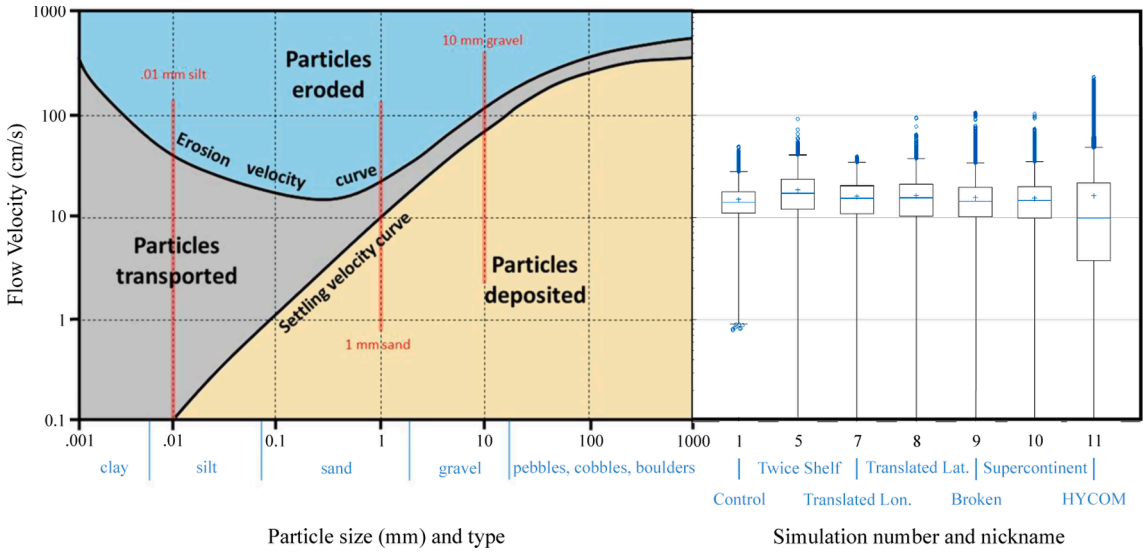

Fig. 8. Distributions of *A* in the continental shelves compared with the Hjulström particle flow diagram (Earle, 2015). **Description**: The axes of the original flow diagram have been reformatted and the image has been placed to the left of a series of box and whisker plots. Each box spans vertically from the 25th to 75th percentiles, with whiskers reaching to the most extreme non-outlier data. Outliers are plotted individually. (Lower extremes and outliers for all simulations other than the control reach 0 cm/s and fall outside the plot range. In this study, our primary concern is with upper velocity extremes. For full rendering of lower tails, refer to the linear boxplots in supplemental figure S4).

the Archean sedimentary record on the Canadian Shield is characterized by texturally immature rocks consistent with 'unstable' transport and turbidity currents and Eriksson et al. (1998) documents thick sandstone sequences all over the globe that are associated with tidal depositional settings that lack small-scale sedimentary features (i.e., they lack evidence for low energy transport processes). Both of those sets of results are consistent with our model results here that suggest the potential for eroding both larger clasts and more clastic material in response to higher tidal velocities. The simulation results suggest that the mid-Archean may have experienced tidal erosion and particle transport patterns that are not achievable in the present day. To assess this quantitatively, more simulations with realistic, higher resolution coastlines would need to be performed.

4.5. Simpson-Hunter parameter (S) in the continental shelves

The Simpson-Hunter parameter (Simpson and Hunter, 1974) determines the existence of tidal mixing fronts and is given by

$$S = \log_{10}\left(\frac{h}{u^3}\right) \tag{3}$$

where h is the depth of the water column, $u = A$ (Section 4.4) is the depth-averaged tidal velocity (Timko et al., 2019), and the air-sea heat flux, Q, is assumed to be constant. For all computations of S in this paper, the units for h and u are taken to be m and m s^{-1}, respectively. Under these conditions, the critical value for S is about 2.7 (Bowers and Simpson, 1987). For each of the simulations in Fig. 9, the critical value is represented as a dashed vertical line on the plot, and the mean value is shown as a solid line. Because small values of S represent areas of tidal mixing, here we are calculating the percentages of values that fall below

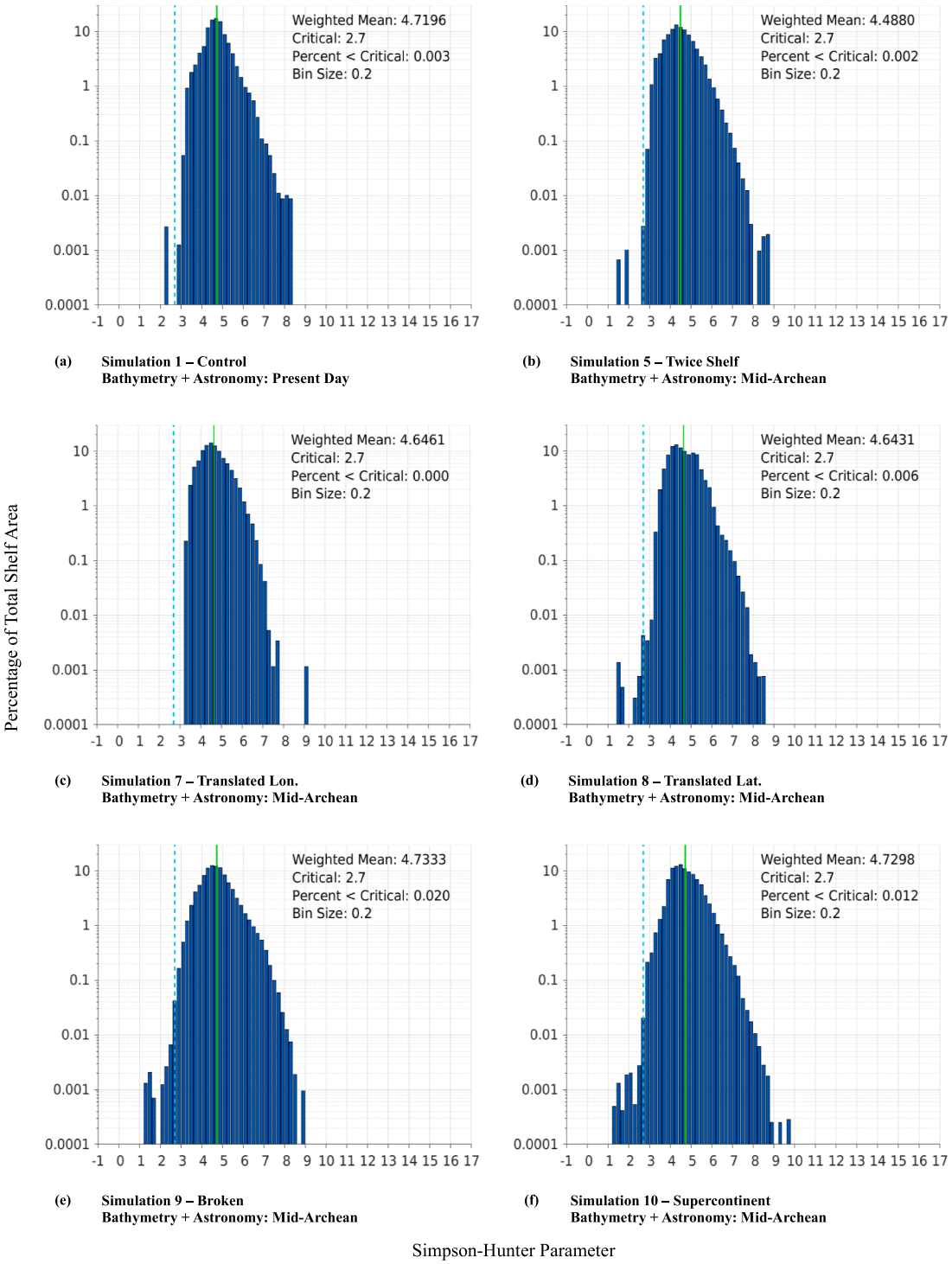

Fig. 9. Simpson-Hunter parameter in the continental shelves.

the critical line. Note that when the text refers to "areas" or "locations" with small or subcritical S values, the language refers to horizontal positions along the grid where tidal mixing fronts could have been present, as inferred by tidal velocities observed in the one-layer model. Such wording does not refer to vertically mixed area, as single-layer simulations do not simulate tidal mixing. Doing so would require a multi-layer model.

Not all of the mid-Archean simulations result in more values of S below the critical value than the control; the results appear to be highly dependent on bathymetry. The two simulations that stand out as having significantly more S values below 2.7 are number 9 (the "island-arc" world) and number 10 (the "supercontinent" world). There is some initial indication that with these continental configurations, tidal mixing conditions could have been more favorable than in the present day. However, simulations 5 and 7 indicate that less favorable tidal mixing conditions in the continental shelves were also possible, depending on the bathymetry.

Comparing against the HYCOM results (Fig. 10) we see that the idealized geometries yield non-continuous distributions of S values in the lower extremes, whereas the HYCOM simulation indicates that real

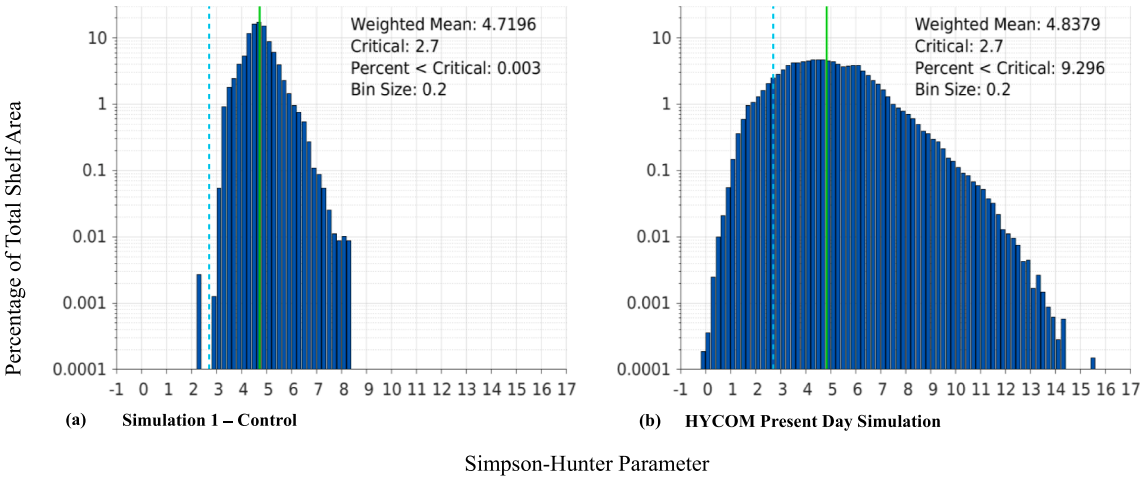

Fig. 10. Simpson-Hunter parameter in the continental shelves (control vs. HYCOM).

bathymetries are likely to yield S distributions that are continuous in the lower tails. Perhaps then, the better statistic to consider here is the lowest achieved value of S in each simulation, in which case we see more favorable tidal mixing conditions in all but simulation 7 (Fig. 9).

A limitation of the conclusions above is that the idealized simulations provide very few below-critical S values for comparison. In every one of the simulations in Fig. 9, there are relatively few values that fall below the critical line (0.02% or less in all simulations). Any conclusions drawn about trends from such a small sample of outliers have an inherently low confidence level. We can judge from Fig. 10 that the presence of low S values is highly dependent on having a realistic coastline. In the present-day HYCOM simulation (Fig. 10b), the number of below-critical S values is over 9% (about 3,098 times more than in the idealized control). Therefore, it seems that more simulations with realistic bays and shelves are needed to determine if tidal mixing fronts really were more prevalent in the mid-Archean than they are today, although our results provide some initial indication that this was possible.

4.6. *Effects of water volume and maximum depth*

As discussed in Section 3.1, the idealized bathymetries used in the "representative" simulations were constructed by adjusting the ocean floor depth—and therefore, the water volume—in order to hold the average depth and other characteristics constant as the land area was repositioned. It was hypothesized that these changes to water volume and ocean floor depth would have a relatively small impact on tidal characteristics in the shelf regions. In this section, we evaluate the validity of that assumption by comparing transitional simulations 3 and 4, which differ only by ocean floor depth. Recall from Section 3.1 that the bathymetry in simulation 4 has a shallower ocean floor and a 2.8% decrease in water volume compared to the bathymetry in simulation 3.

Histograms of SSH amplitudes in the shelves (Fig. 11) reveal similar distributions between the two scenarios, but in the simulation with decreased water volume, the mean SSH amplitude has decreased by ~3% and the maximum SSH amplitude has fallen by ~0.1 m.

Histograms of A in the continental shelves (Fig. 12) reveal slightly lower summary statistics in the case of decreased water volume. The mean value of A drops by ~3% and the maximum parcel velocity achieved decreases by ~0.02 m s^{-1}.

Simpson-Hunter statistics are also similarly impacted by the change in water volume (Fig. 13). In this case, the decrease in water volume results in an increased mean of ~1% and a decrease in sub-critical values of about 37%, suggesting a decrease in the shelf area where tidal mixing fronts are present.

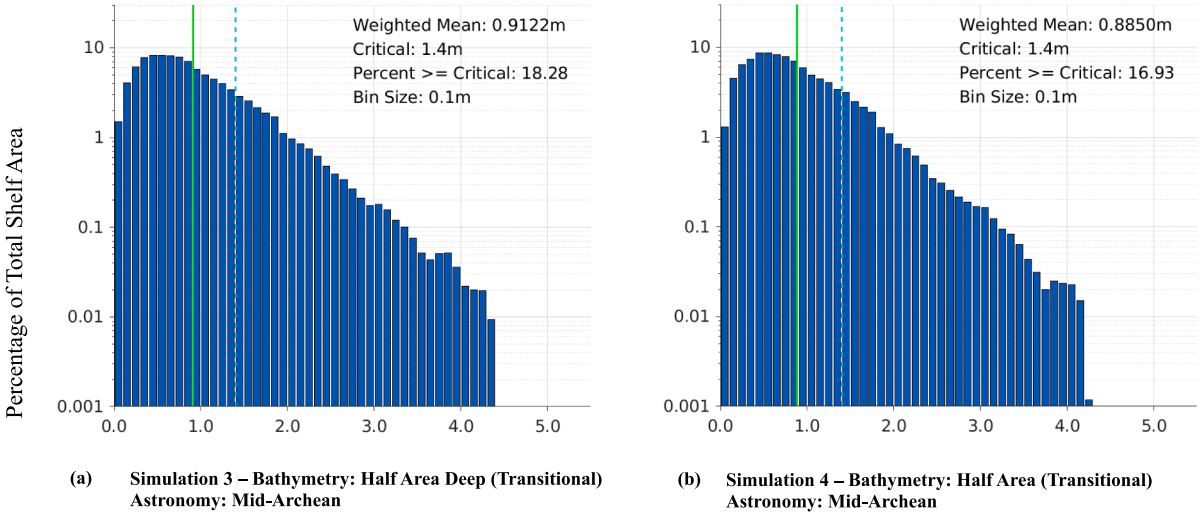

Fig. 11. SSH amplitudes in the continental shelves (ocean depth comparison).

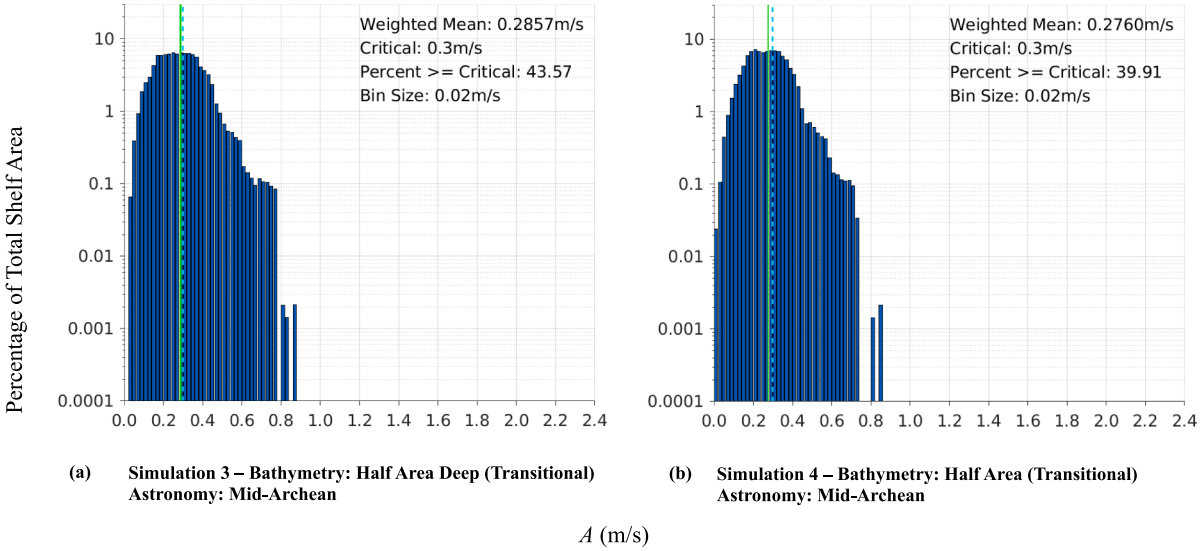

Fig. 12. Parcel velocity semi-major axis values (A) in the continental shelves (ocean depth comparison).

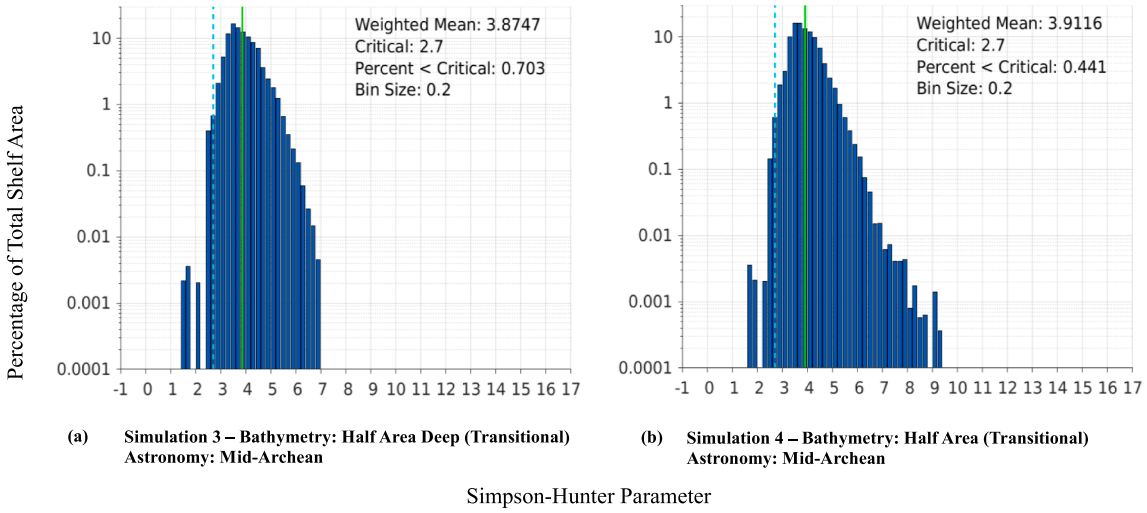

Fig. 13. Simpson-Hunter parameter in the continental shelves (ocean depth comparison).

Apparently, the effect of increased water volume in the ocean is to slightly increase tidal amplitudes, velocities, and mixing fronts in the continental shelves. However, with a difference in ocean volume of < 3%, these differences are relatively small when compared to the impact of other bathymetry characteristics, such as continental placement and resonance conditions. Water volumes in our study are consistent amongst the mid-Archean representative simulations but greater than that of the present day control by ~13.8%. Therefore, if we were to assume that the water volume in the mid-Archean oceans was the same as the present day, it's possible that the extreme values for SSH, A, and S obtained from Sections 4.3 to 4.5 are currently slightly inflated. That being said, it is unknown whether the total water volume in the mid-Archean oceans was greater than or less than that of the present day earth, as the sea level depends on factors such as the temperature of the Earth's surface and the density structure of the mantle, many of which are still topics of research.

4.7. Implications for Archean biogeochemistry

The mid-Archean to Neoarchean was generally characterized by high atmospheric CO_2 levels (e.g., Driese et al., 2011; Kanzaki and Murakami, 2015), which in turn, should have resulted in high weathering rates for any surface rocks that were exposed to the atmosphere (e.g., Kump et al., 2000; Zaharescu et al., 2020). Previous work on the Paleoproterozoic and Mesoproterozoic by Mitchell and Sheldon (2016) validated this relationship by comparing reconstructed CO_2 levels and paleo-delta sediment chemistry. In addition, mid-Archean crust and weathering products (Beaty and Planavsky, 2021; Lipp et al., 2021; Sheldon et al., 2021; Dzombak and Sheldon, 2022) all had comparable inventories of key nutrient elements such as Ca, K, Na, and P, and higher levels of Fe and Mg relative to both average crustal compositions for the past 4 Ga overall and today (e.g. Dzombak and Sheldon, 2020). Given that atmospheric O_2 was also much lower (various, e.g., Lyons et al., 2014), the redox state of elements like Fe and Cr was also different in the weathering product, resulting in significantly increased dissolved transport of redox sensitive bio-available metals (e.g., Colwyn et al., 2019). For example, mid-Archean paleosols have a much higher proportion of Fe^{2+} than even other pre-Great Oxidation Event paleosols, suggesting efficient delivery of Fe^{2+} to the oceans at that time (Sheldon et al., 2021). Putting these ideas together, the nutrient flux to drive microbial metabolic activity in the Archean was controlled by the weatherable land area as well as the weathering intensity.

As we have demonstrated herein, even under simplified continental and coastal geometries, tidal forcing and other key parameters like water parcel velocity and SSH that play key roles in controlling sediment (and nutrient delivery) in the Archean equaled or exceeded present-day forcing. To account for the simplified geometry, we have compared the control scenario 1 to modern HYCOM results to determine the appropriate Archean scaling factors, roughly estimating that SSH would have been 2.5x higher and water parcel velocity 4.5x higher. Higher velocities coupled with a shorter day length would have resulted in significantly increased seabed exposure and significantly increased weathering of seabed rocks and sediments, including the potential to transport much larger sediments than at present. While more work is needed to validate the result, comparison of the Simpson-Hunter parameter for tidal mixing between those two scenarios also provides some evidence for substantially more tidal mixing fronts in the Archean than at present for some continental geometries, such as the "island-arc" world and the supercontinent model. In these cases, results suggest that nutrients derived from the continents or continental shelf could also have been better mixed to greater depths and further off shore (Fig. 9). Given that the biological pump is most efficient under low O_2 conditions as in the Archean (Fakhraee et al., 2020), this enhanced flux of tidally derived nutrients may also have played an important role in maintaining the global carbon cycle, but further work is needed to couple biogeochemical and tidal models to understand this relationship quantitatively rather than qualitatively. A second potential impact of increased tidal mixing would be that it could offer some mechanistic support for models of BIF formation based on observations of rhythmic switching between Fe-rich and Fe-poor strata (Bontognali et al., 2013; Ojakangas, 1983; Ojakangas and Ojakangas, 2010; Walker and Zahnle, 1986; Watchorn, 1980), especially if coupled with extreme tidal velocities and SSH capable of weathering and transporting more material.

All of the Archean scenarios resulted in higher mean water parcel velocities in the shelf regions than in the default model, and most resulted in larger extreme values there as well. These findings suggest that the combined effect of mid-Archean astronomical conditions, reduced land area, and wider shelf area (as in low freeboard continents) tend to increase tidal velocities in the continental shelves. Yet, the significance of this increase is highly dependent on the position and number of the continents, and these differences are important to consider as plate tectonic reconstructions improve. Within the various Archean continental configurations, one of the simulations that most amplified the enhanced tidal velocities was the scenario with small fragmented continents. This bathymetry is also one of the most realistic based upon geodynamic considerations (Flament et al., 2008; Rey and Coltice, 2008). This suggests that regions with more rapid BIF deposition may have existed on the margins of small continents. Future work is needed to validate this result using more realistic coastlines and a wider variety of "island-arc" geometries.

5. Conclusion

To examine the potential role of tides in Archean biogeochemistry, we performed a number of simulations using realistically increased tidal forcing and idealized geometries. To quantify the importance of geometry, we also compared those results to a modern tidal scenario (HYCOM). We find through those comparisons the distribution of key parameters in shallow shelf areas including dissipation, SSH, tidal velocity parameter A, and the Simpson-Hunter parameter S include, in many cases, more extreme values under Archean tidal forcing. Further, by comparing the idealized control scenario with HYCOM, we find that the idealized geometries suppress those extreme results relative to HYCOM, indicating that Archean extremes would have been much higher than those measured here. For example, if the scaling indicated by that comparison is reasonably accurate, then A could have exceeded 4 m s^{-1}, which would have resulted in the potential erosion and transport of materials up to small boulders in size. Further, the SSH amplitude extremes in the Archean, when coupled with the shorter tidal period, would have resulted in a much higher frequency and magnitude of seabed exposure. While models with more realistic coastlines are still needed, Archean conditions also may have been more favorable for tidally induced mixing fronts than present conditions based upon the Simpson-Hunter parameter results, particularly for some continental geometries. In the absence of other potential amplifiers of weathering intensity (e.g., land plants), these results suggest that the stronger tidal forcing on the early Earth likely played a key role in nutrient transport and delivery to shelf areas as well as transport and delivery of those nutrients from the shallowest part of the shelf to deeper parts of the shelf. Collectively, these results point to the importance of stronger tidal forcing on the early Earth as a driver of biogeochemical cycling.

CRediT authorship contribution statement

Eliana B. Crawford: Methodology, Software, Validation, Formal analysis, Investigation, Data curation, Writing – original draft, Visualization, Project administration. **Brian K. Arbic:** Conceptualization, Methodology, Resources, Writing – review & editing, Supervision, Funding acquisition, Project administration. **Nathan D. Sheldon:** Conceptualization, Methodology, Writing – review & editing. **Joseph K. Ansong:** Software, Resources, Supervision. **Patrick G. Timko:** Investigation, Data curation.

Declaration of Competing Interest

The authors declare that they have no known competing financial interests or personal relationships that could have appeared to influence the work reported in this paper.

Acknowledgements

EBC would like to thank Houraa Daher, who provided insight during the model analysis phase, as well as Benjamin Schumacher at Kenyon College for his insight into the single layer tidal equations used by MOM6. EBC also thanks all of the members of the Physical Oceanography lab at the University of Michigan for constructive feedback and criticism: Conrad Luecke, Paige Martin, Amanda O'Rourke, Molly Range, and Anna Savage. EBC, JKA, and BKA gratefully acknowledge Mike Messina for support of the numerical simulations and data analysis, which were carried out on the supercomputer provided by the University of Michigan Office of Research Cyberinfrastructure (ORCI).

Funding

JKA and BKA acknowledge funding support from the University of Michigan Associate Professor Support Fund, supported by the Margaret and Herman Sokol Faculty Awards, and from National Science Foundation (NSF) grants OCE-0968783 and OCE-1351837. EBC and BKA acknowledge a Research Experience for Undergraduates Supplement to OCE-1351837.

Data Availability

All of the data files needed to produce plots in this paper can be found at https://doi.org/10.7910/DVN/A32CT4. The repository containing code to produce the plots in this paper can be found at https://github.com/crawforde/tide-simulation-plots.

Appendix A. Supplementary Material

Supplementary data to this article can be found online at https://doi.org/10.1016/j.precamres.2022.106799.

References

Arbic, B.K., Garner, S.T., Hallberg, R.W., Simmons, H.L., 2004. The accuracy of surface elevations in forward global barotropic and baroclinic tide models. Deep-Sea Res. II 51 (25-26), 3069–3101. https://doi.org/10.1016/j.dsr2.2004.09.014.

Arbic, B.K., Karsten, R.H., Garrett, C., 2009. On tidal resonance in the global ocean and the back-effect of coastal tides upon open-ocean tides. Atmosphere-Ocean 47, 239–266. https://doi.org/10.3137/OC311.2009.

Arbic, B.K., St-Laurent, P., Sutherland, G., Garrett, C., 2007. On the resonance and influence of tides in Ungava Bay and Hudson Strait. Geophys. Res. Lett. 34, L17606. https://doi.org/10.1029/2007GL030845.

Bartlett, B.C., Stevenson, D.J., 2016. Analysis of a Precambrian resonance-stabilized day length. Geophys. Res. Lett. 43 (11), 5716–5724. https://doi.org/10.1002/2016GL068912.

Beaty, B.J., Planavsky, N.J., 2021. A 3 b.y. record of a biotic influence on terrestrial weathering. Geology 49 (4), 407–411. https://doi.org/10.1130/G47986.1.

Behrenfeld, M.J., O'Malley, R.T., Siegel, D.A., McClain, C.R., Sarmiento, J.L., Feldman, G.C., Milligan, A.J., Falkowski, P.G., Letelier, R.M., Boss, E.S., 2006. Climate-driven trends in contemporary ocean productivity. Nature 444 (7120), 752–755. https://doi.org/10.1038/nature05317.

Bekker, A., Slack, J.F., Planavsky, N.J., Krapez, B., Hofmann, A., Konhauser, K.O., Rouxel, O.J., 2010. Iron formation: the sedimentary product of a complex interplay among mantle, tectonic, oceanic, and biospheric processes. Econ. Geol. 105 (3), 467–508. https://doi.org/10.2113/gsecongeo.105.3.467.

Bills, B.G., Ray, R.D., 1999. Lunar orbital evolution: a synthesis of recent results. Geophys. Res. Lett. 26 (19), 3045–3048. https://doi.org/10.1029/1999GL008348.

Bjerrum, C.J., Canfield, D.E., 2002. Ocean productivity before about 1.9 Gyr ago limited by phosphorus adsorption onto iron oxides. Nature 417, 159–162. https://doi.org/10.1038/417159a.

Blackledge, B.W., Green, J.A.M., Barnes, R., Way, M.J., 2020. Tides on other Earths: Implications for exoplanet and palaeo-tidal simulations. Geophysical Research Letters 47, e2019GL085746. https://doi.org/10.1029/2019GL085746.

Bontognali, T.R.R., Fischer, W.W., Föllmi, K.B., 2013. Siliciclastic associated banded iron formations from the 3.2 Ga Moodies Group, Barberton Greenstone Belt, South Africa. Precambrian Res. 226, 116–124. https://doi.org/10.1016/j.precamres.2012.12.003.

Bowers, D.G., Brubaker, J.M., 2010. Tidal amplification of seabed light. J. Geophys. Res. 115 (C9), C09008. https://doi.org/10.1029/2009JC005785.

Bowers, D.G., Simpson, J.H., 1987. Mean position of tidal fronts in European Shelf Sea. Cont. Shelf Res. 7, 35–44. https://doi.org/10.1016/0278-4343(87)90062-8.

Capitanio, F.A., Nebel, O., Cawood, P.A., Weinberg, R.F., Chowdhury, P., 2019. Reconciling thermal regimes and tectonics of the early Earth. Geology 47, 923–927. https://doi.org/10.1130/G46239.1.

Cartwright, D.E., 1999. Tides: A Scientific History. Cambridge University Press, Cambridge.

Cawood, P.A., Hawkesworth, C.J., Pisarevsky, S.A., Dhuime, B., Capitanio, F.A., Nebel, O., 2018. Geological archive of the onset of plate tectonics. Philos. Trans. R. Soc. A. 376 (2132), 20170405. https://doi.org/10.1098/rsta.2017.0405.

Chassignet, E.P., Hurlburt, H.E., Metzger, E.J., Smedstad, O.M., Cummings, J.A., Halliwell, G.R., Bleck, R., Baraille, R., Wallcraft, A.J., Lozano, C., Tolman, H.L., Srinivasan, A., Hankin, S., Cornillon, P., Weisberg, R., Barth, A., He, R., Werner, F., Wilkin, J., 2009. US GODAE: Global ocean prediction with the HYbrid Coordinate Ocean Model (HYCOM). Oceanography. 22 (2), 64–75. https://doi.org/10.5670/oceanog.2009.39.

Chen, C.-T.A., Borges, A.V., 2009. Reconciling opposing views on carbon cycling in the coastal ocean: continental shelves as sinks and near-shore ecosystems as sources of atmospheric CO_2. Deep Sea Res. II: Topics Studies Oceanogr. 56 (8–10), 578–590. https://doi.org/10.1016/j.dsr2.2009.01.001.

Colwyn, D.A., Sheldon, N.D., Maynard, J.B., Gaines, R., Hofmann, A., Wang, X., Gueguen, B., Asael, D., Reinhard, C.T., Planavsky, N.J., 2019. A paleosol record of the evolution of Cr redox cycling and evidence for an increase in atmospheric oxygen during the Neoproterozoic. Geobiology 17 (6), 579–593. https://doi.org/10.1111/gbi.12360.

Condie, K.C., 1997. Plate Tectonics and Crustal Evolution, fourth ed. Butterworth-Heinemann, Jordan Hill, Oxford.

Daher, H., Arbic, B.K., Williams, J.G., Ansong, J.K., Boggs, D.H., Müller, M., Schindelegger, M., Austermann, J., Cornuelle, B.D., Crawford, E.B., Fringer, O.B., Lau, H.C.P., Lock, S.J., Maloof, A.C., Menemenlis, D., Mitrovica, J.X., Green, J.A.M., Huber, M., 2021. Long-term Earth-Moon evolution with high-level orbit and ocean tide models. J. Geophys. Res.: Planets 126, e2021JE006875. https://doi.org/10.1029/2021JE006875.

Dickey, J.O., Bender, P.L., Faller, J.E., Newhall, X.X., Ricklefs, R.L., Ries, J.G., Shelus, P.J., Veillet, C., Whipple, A.L., Wiant, J.R., Williams, J.G., Yoder, C.F., 1994. Lunar laser ranging: a continuing legacy of the Apollo program. Science 265 (5171), 482–490. https://doi.org/10.1126/science.265.5171.482.

Driese, S.G., Jirsa, M.A., Ren, M., Brantley, S.L., Sheldon, N.D., Parker, D., Schmitz, M., 2011. Neoarchean paleoweathering of tonalite and metabasalt: implications for reconstructions of 2.69 Ga early terrestrial ecosystems and paleoatmospheric chemistry. Precambrian Res. 189 (1–2), 1–17. https://doi.org/10.1016/j.precamres.2011.04.003.

Dzombak, R.M., Sheldon, N.D., 2020. Weathering intensity and presence of vegetation are key controls on soil phosphorus concentrations: implications for past and future terrestrial ecosystems. Soil Syst. 4, 73. https://doi.org/10.3390/soilsystems4040073.

Dzombak, R.M., Sheldon, N.D., 2022. Terrestrial records of weathering indicate three billion years of dynamic equilibrium. Gondwana Res. 109, 376–393. https://doi.org/10.1016/j.gr.2022.05.009.

Earle, S., 2015. Stream Erosion and Deposition, Figure. 13.16., in: Physical Geology, second ed. BCcampus, Victoria, B.C. Used under a CC BY 4.0 License. Available from: https://opentextbc.ca/geology/.

Egbert, G.D., Ray, R.D., 2000. Significant dissipation of tidal energy in the deep ocean inferred from satellite altimeter data. Nature 405 (6788), 775–778. https://doi.org/10.1038/35015531.

Egbert, G.D., Ray, R.D., 2003. Semi-diurnal and diurnal tidal dissipation from TOPEX/Poseidon altimetry. Geophys. Res. Lett. 30 (17), 1907. https://doi.org/10.1029/2003GL017676.

Egbert, G.D., Ray, R.D., Bills, B.G., 2004. Numerical modeling of the global semidiurnal tide in the present day and in the Last Glacial Maximum. J. Geophys. Res. Oceans 109, C03003. https://doi.org/10.1029/2003JC001973.

Emery, K.O., Uchupi, E. (Eds.), 1984. The Geology of the Atlantic Ocean. Springer New York, New York, NY.

Eriksson, P.G., Condie, K.C., Tirsgaard, H., Mueller, W.U., Altermann, W., Miall, A.D., Aspler, L.B., Catuneanu, O., Chiarenzelli, J.R., 1998. Precambrian clastic sedimentation systems. Sed. Geol. 120 (1-4), 5–53. https://doi.org/10.1016/S0037-0738(98)00026-8.

Fairbridge, R.W., Bourgeois, J., 1978. Submarine (bathyal) slope sedimentation. In: Fairbridge, R.W., Bourgeois, J. (Eds.), Encyclopedia of Sedimentology. Hutchinson & Ross Inc., Stroudsburg, Dowden, pp. 774–777.

Fakhraee, M., Planavsky, N.J., Reinhard, C.T., 2020. The role of environmental factors in the long-term evolution of the marine biological pump. Nat. Geosci. 13 (12), 812–816. https://doi.org/10.1038/s41561-020-00660-6.

Fiorella, R.P., Sheldon, N.D., 2017. Equable end Mesoproterozoic climate in the absence of high CO2. Geology 45 (3), 231–234. https://doi.org/10.1130/G38682.1.

Flament, N., Coltice, N., Rey, P.F., 2008. A case for late-Archaean continental emergence from thermal evolution and hypsometry. Earth Planet. Sci. Lett. 275, 326–336. https://doi.org/10.1016/j.epsl.2008.08.029.

Gibling, M.R., Davies, N.S., 2012. Palaeozoic landscapes shaped by plant evolution. Nat. Geosci. 5 (2), 99–105. https://doi.org/10.1038/ngeo1376.

Green, J.A.M., Huber, M., 2013. Tidal dissipation in the early Eocene and implications for ocean mixing. Geophys. Res. Lett. 40 (11), 2707–2713. https://doi.org/10.1002/grl.50510.

Green, J.A.M., Huber, M., Waltham, D., Buzan, J., Wells, M., 2017. Explicitly modelled deep-time tidal dissipation and its implication for lunar history. Earth Planet. Sci. Lett. 461, 46–53. https://doi.org/10.1016/j.epsl.2016.12.038.

Gross, G.A., 1980. A classification of iron-formations based on depositional environments. Can. Mineral. 18, 215–222.

Heezen, B.C., Tharp, M., Ewing, M., 1959. The Floors of the Oceans. Geological Society of America Special Paper 65. Boulder, Colorado.

Hendershott, M.C., 1972. The effects of solid earth deformation on global ocean tides. Geophys. J. R. Astron. Soc. 29 (4), 389–402. https://doi.org/10.1111/j.1365-246X.1972.tb06167.x.

Herzberg, C., Condie, K., Korenaga, J., 2010. Thermal history of the Earth and its petrological expression. Earth Planet. Sci. Lett. 292 (1-2), 79–88. https://doi.org/10.1016/j.epsl.2010.01.022.

Holder, R.M., Viete, D.R., Brown, M., Johnson, T.E., 2019. Metamorphism and the evolution of plate tectonics. Nature 572 (7769), 378–381. https://doi.org/10.1038/s41586-019-1462-2.

Howarth, R.W., 1988. Nutrient limitation of net primary production in marine ecosystems. Annu. Rev. Ecol. 19 (1), 89–110. https://doi.org/10.1146/annurev.es.19.110188.000513.

Jayne, S.R., St Laurent, L.C., 2001. Parameterizing tidal dissipation over rough topography. Geophys. Res. Lett. 28, 811–814. https://doi.org/10.1029/2000gl012044.

Johnson, J.E., Muhling, J.R., Cosmidis, J., Rasmussen, B., Templeton, A.S., 2018. Low-Fe (III) greenalite was a primary mineral from Neoarchean oceans. Geophys. Res. Lett. 45 (7), 3182–3192. https://doi.org/10.1002/2017GL076311.

Jones, C., Nomosatryo, S., Crowe, S.A., Bjerrum, C.J., Canfield, D.E., 2015. Iron oxides, divalent cations, silica, and the early Earth phosphorus crisis. Geology 43 (2), 135–138. https://doi.org/10.1130/G36044.1.

Kanzaki, Y., Murakami, T., 2015. Estimates of atmospheric CO_2 in the Neoarchean-Paleoproterozoic from paleosols. Geochim. Cosmochim. Acta 159, 190–219. https://doi.org/10.1016/j.gca.2015.03.011.

Kappler, A., Pasquero, C., Konhauser, K.O., Newman, D.K., 2005. Deposition of banded iron formations by anoxygenic phototrophic Fe(II)-oxidizing bacteria. Geology 33 (11), 865–868. https://doi.org/10.1130/G21658.1.

Konhauser, K.O., 1998. Diversity of bacterial iron mineralization. Earth Sci. Rev. 43 (3-4), 91–121. https://doi.org/10.1016/S0012-8252(97)00036-6.

Konhauser, K.O., Hamade, T., Raiswell, R., Morris, R.C., Ferris, F.G., Southam, G., Canfield, D.E., 2002. Could bacteria have formed Precambrian banded iron formations? Geology 30, 1079–1082. https://doi.org/10.1130/0091-7613(2002)030<1079:CBHFTP>2.0.CO;2.

Konhauser, K.O., Amskold, L., Lalonde, S.V., Posth, N.R., Kappler, A., Anbar, A., 2007. Decoupling photochemical Fe(II) oxidation from shallow-water BIF deposition. Earth Planet. Sci. Lett. 258 (1-2), 87–100. https://doi.org/10.1016/j.epsl.2007.03.026.

Konhauser, K.O., Planavsky, N.J., Hardisty, D.S., Robbins, L.J., Warchola, T.J., Haugaard, R., Lalonde, S.V., Partin, C.A., Oonk, P.B.H., Tsikos, H., Lyons, R.W., Bekker, A., Johnson, C.M., 2017. Iron formations: a global record of Neoarchean to Palaeoproterozoic environmental history. Earth Sci. Rev. 172, 140–177. https://doi.org/10.1016/j.earscirev.2017.06.012.

Kump, L.R., Brantley, S.L., Arthur, M.A., 2000. Chemical weathering, atmospheric CO_2, and climate. Ann. Rev. Earth Planetary Sci. 28 (1), 611–667. https://doi.org/10.1146/annurev.earth.28.1.611.

Lambeck, K., 1980. The Earth's Variable Rotation: Geophysical Causes and Consequences. Cambridge University Press, Cambridge. https://doi.org/10.1017/CBO9780511569579.
Lenton, T.M., Daines, S.J., 2018. The effects of marine eukaryote evolution on phosphorus, carbon and oxygen cycling across the Proterozoic-Phanerozoic transition. Emerging Topics Life Sci 2, 267–278. https://doi.org/10.1042/ETLS20170156.
Lenton, T.M., Daines, S.J., 2017. Matworld – the biogeochemical effects of early life on land. New Phytol. 215 (2), 531–537. https://doi.org/10.1111/nph.14338.
Lipp, A.G., Shorttle, O., Sperling, E.A., Brocks, J.J., Cole, D.B., Crockford, P.W., Del Mouro, L., Dewing, K., Dornbos, S.Q., Emmings, J.F., Farrell, U.C., Jarrett, A., Johnson, B.W., Kabanov, P., Keller, C.B., Kunzmann, M., Miller, A.J., Mills, N.T., O'Connell, B., Peters, S.E., Planavsky, N.J., Ritzer, S.R., Schoepfer, S.D., Wilby, P.R., Yang, J., 2021. The composition and weathering of the continents over geologic time. Geochem. Persp. Let. 17, 21–26. https://doi.org/10.7185/geochemlet.2109.
Luskin, C., Wilson, A., Gold, D., Hofmann, A., 2019. The Pongola Supergroup: Mesoarchaean deposition following Kaapvaal Craton stabilization. In: Kröner, A., Hofmann, A. (Eds.), The Archaean Geology of the Kaapvaal Craton, Southern Africa. Regional Geology Reviews. Springer, Cham. https://doi.org/10.1007/978-3-319-78652-0_9.
Lyons, T.W., Reinhard, C.T., Planavsky, N.J., 2014. The rise of oxygen in Earth's early ocean and atmosphere. Nature 506 (7488), 307–315. https://doi.org/10.1038/nature13068.
Mitchell, R.L., Sheldon, N.D., 2016. Sedimentary provenance and weathering processes in the 1.1 Ga Midcontinental Rift of the Keweenaw Peninsula, Michigan, USA. Precambr. Res. 275, 225–240. https://doi.org/10.1016/j.precamres.2016.01.017.
Moore, C.M., Mills, M.M., Arrigo, K.R., Berman-Frank, I., Bopp, L., Boyd, P.W., Galbraith, E.D., Geider, R.J., Guieu, C., Jaccard, S.L., Jickells, T.D., La Roche, J., Lenton, T.M., Mahowald, N.M., Marañón, E., Marinov, I., Moore, J.K., Nakatsuka, T., Oschlies, A., Saito, M.A., Thingstad, T.F., Tsuda, A., Ulloa, O., 2013. Processes and patterns of oceanic nutrient limitation. Nat. Geosci. 6 (9), 701–710. https://doi.org/10.1038/ngeo1765.
Müller, M., 2007. The free oscillations of the world ocean in the period range 8 to 165 hours including the full loading effect. Geophys. Res. Lett. 34, L05606. https://doi.org/10.1029/2006GL028870.
Müller, M., 2008. Synthesis of forced oscillations, Part I: Tidal dynamics and the influence of the loading and self-attraction effect. Ocean Model. 20 (3), 207–222. https://doi.org/10.1016/j.ocemod.2007.09.001.
Müller, M., 2009. A Large Spectrum of Free Oscillations of the World Ocean Including the Full Ocean Loading and Self-attraction Effects. In: Müller, M. (Ed.), Hamburg Studies on Maritime Affairs, 14. Springer Berlin, Heidelberg. https://doi.org/10.1007/978-3-540-85576-7.
Muller-Karger, F.E., Varela, R., Thunell, R., Luerssen, R., Hu, C., Walsh, J.J., 2005. The importance of continental margins in the global carbon cycle. Geophys. Res. Lett. 32, L01602. https://doi.org/10.1029/2004GL021346.
Munk, W.H., MacDonald, G.J.F., 1960. The Rotation of the Earth: A Geophysical Discussion. Cambridge University Press, London. https://doi.org/10.1017/S0016756800036578.
Ojakangas, G.W., Ojakangas, R.W., 2010. Lunisolar Tidal Signatures in the ~1.9 Ga Pokegama Formation, Northeastern Minnesota: Implications for the Lunar Orbit. Minnesota Geological Survey Report of Investigations 67, 1–11. http://hdl.handle.net/11299/96722.
Ojakangas, R.W., 1983. Tidal deposits in the early Proterozoic basin of the Lake Superior region—The Palms and Pokegama Formations: Evidence for subtidal-shelf deposition of Superior-type banded iron-formation. Geol. Soc. Am. 160, 49–66. https://doi.org/10.1130/MEM160-p49.
Olson, S.L., Kump, L.R., Kasting, J.F., 2013. Quantifying the areal extent and dissolved oxygen concentrations of Archean oxygen oases. Chem. Geol. 362, 35–43. https://doi.org/10.1016/j.chemgeo.2013.08.012.
Planavsky, N.J., Rouxel, O.J., Bekker, A., Lalonde, S.V., Konhauser, K.O., Reinhard, C.T., Lyons, T.W., 2010. The evolution of the marine phosphate reservoir. Nature 467 (7319), 1088–1090. https://doi.org/10.1038/nature09485.
Platzman, G.W., 1984. Normal modes of the World Ocean. Part IV: synthesis of diurnal and semidiurnal tides. J. Phys. Oceanogr. 14, 1532–1550. https://doi.org/10.1175/1520-0485(1984)014<1532:NMOTWO>2.0.CO;2.
Platzman, G.W., 1991. Tidal evidence for ocean normal modes. In: Parker, B.B. (Ed.), Tidal Hydrodynamics. John Wiley and Sons, pp. 13–26.
Posth, N.R., Canfield, D.E., Kappler, A., 2014. Biogenic Fe(III) minerals: from formation to diagenesis and preservation in the rock record. Earth Sci. Rev. 135, 103–121. https://doi.org/10.1016/j.earscirev.2014.03.012.
Posth, N.R., Konhauser, K.O., Kappler, A., 2011. Banded Iron Formations. In: Encyclopedia of Geobiology. Springer, Netherlands, pp. 92–103.
Posth, N.R., Konhauser, K.O., Kappler, A., 2013. Microbiological processes in banded iron formation deposition. Sedimentology 60 (7), 1733–1754. https://doi.org/10.1111/sed.12051.
Pratt, B.R., 2001. Oceanography, bathymetry and syndepositional tectonics of a Precambrian intracratonic basins: integrating sediments, storms, earthquakes and tsunamis in the Belt Supergroup (Helena Formation, ca. 1.45 Ga), western North America. Sed. Geol. 141–142, 371–394. https://doi.org/10.1016/S0037-0738(01)00083-5.
Pugh, D.T., 1987. Tides, Surges and Mean Sea-level: A Handbook for Scientists and Engineers. Wiley, Chichester. https://doi.org/10.1111/j.1365-246X.1988.tb06710.x.
Ray, R.D., 1998. Ocean self-attraction and loading in numerical tide models. Mar. Geod. 21, 181–192. https://doi.org/10.1080/01490419809388134.
Reinhard, C.T., Planavsky, N.J., Gill, B.C., Ozaki, K., Robbins, L.J., Lyons, T.W., Fischer, W.W., Wang, C., Cole, D.B., Konhauser, K.O., 2017. Evolution of the global phosphorus cycle. Nature 541 (7637), 386–389. https://doi.org/10.1038/nature20772.
Rey, P.F., Coltice, N., 2008. Neoarchean lithospheric strengthening and coupling of Earth's geochemical reservoirs. Geology 36, 635–638. https://doi.org/10.1130/G25031A.1.
Robbins, L.J., Funk, S.P., Flynn, S.L., Warchola, T.J., Li, Z., Lalonde, S.V., Rostron, B.J., Smith, A.J.B., Beukes, N.J., de Kock, M.O., Heaman, L.M., Alessi, D.S., Konhauser, K.O., 2019. Hydrogeological constraints on the formation of Palaeoproterozoic banded iron formations. Nat. Geosci. 12 (7), 558–563. https://doi.org/10.1038/s41561-019-0372-0.
Ross, M.N., Schubert, G., 1989. Evolution of the lunar orbit with temperature- and frequency-dependent dissipation. J. Geophys. Res. 94 (B7), 9533–9544. https://doi.org/10.1029/JB094iB07p09533.
Sheldon, N.D., Mitchell, R.L., Dzombak, R.M. (Eds.), 2021. Reconstructing Precambrian pCO_2 and pO_2 Using Paleosols. Cambridge University Press. https://doi.org/10.1017/9781108870962.
Simpson, J.H., Hunter, J.R., 1974. Fronts in the Irish Sea. Nature 250 (5465), 404–406. https://doi.org/10.1038/250404a0.
Smith, R.W., Bianchi, T.S., Allison, M., Savage, C., Galy, V., 2015. High rates of organic carbon burial in fjord sediments globally. Nat. Geosci. 8 (6), 450–453. https://doi.org/10.1038/ngeo2421.
Smith, W.H.F., Sandwell, D.T., 1997. Global sea floor topography from satellite altimetry and ship depth soundings. Science 277 (5334), 1956–1962. https://doi.org/10.1126/science.277.5334.1956.
Stüeken, E.E., Buick, R., Guy, B.M., Koehler, M.C., 2015. Isotopic evidence for biological nitrogen fixation by molybdenum-nitrogenase from 3.2 Gyr. Nature 520, 666–669. https://doi.org/10.1038/nature14180.
Timko, P.G., Arbic, B.K., Hyder, P., Richman, J.G., Zamudio, L., O'Dea, E., Wallcraft, A.J., Shriver, J.F., 2019. Assessment of shelf sea tides and tidal mixing fronts in a global ocean model. Ocean Modeling. 136, 66–84. https://doi.org/10.1016/j.ocemod.2019.02.008.
Hallberg, R. The Modular Ocean Model (MOM). Geophysical Fluid Dynamics Laboratory, NOAA. Available from: <https://www.gfdl.noaa.gov/mom-ocean-model/> (accessed June 2015).
Trendall, A.F., 2002. The significance of iron-formation in the Precambrian stratigraphic record. International Association of Sedimentologists Special Paper 33, 33–66. https://doi.org/10.1002/9781444304312.ch3.
Tyrrell, T., 1999. The relative influences of nitrogen and phosphorus on oceanic primary production. Nature 400 (6744), 525–531. https://doi.org/10.1038/22941.
Van de Kreeke, J., Robaczewska, K., 1993. Tide-induced residual transport of coarse sediment; Application to the EMS estuary. Neth. J. Sea Res. 31 (3), 209–220. https://doi.org/10.1016/0077-7579(93)90022-K.
Walker, J.C.G., Zahnle, K.J., 1986. Lunar nodal tide and distance to the Moon during the Precambrian. Nature 320 (6063), 600–602. https://doi.org/10.1038/320600a0.
Walsh, J.J., 1991. Importance of continental margins in the marine biogeochemical cycling of carbon and nitrogen. Nature 350 (6313), 53–55. https://doi.org/10.1038/350053a0.
Watchorn, M., 1980. Fluvial and tidal sedimentation in the 3000 Ma Mozaan Basin, South Africa. Precambrian Res. 13 (1), 27–42. https://doi.org/10.1016/0301-9268(80)90057-1.
Webb, D.J., 1982. Tides and the evolution of the Earth-Moon system. Geophys. J. Int. 70 (1), 261–271. https://doi.org/10.1111/j.1365-246X.1982.tb06404.x.
Williams, G.E., 1997. Precambrian length of day and the validity of tidal rhythmite paleotidal values. Geophys. Res. Lett. 24 (4), 421–424. https://doi.org/10.1029/97GL00234.
Williams, J.G., Boggs, D.H., 2016. Secular tidal changes in lunar orbit and Earth rotation. Celest. Mech. Dyn. Astron. 126 (1-3), 89–129. https://doi.org/10.1007/s10569-016-9702-3.
Williams, J.G., Sinclair, W.S., Yoder, C.F., 1978. Tidal acceleration of the Moon. Geophys. Res. Lett. 5 (11), 943–946. https://doi.org/10.1029/GL005i011p00943.
Young, G.M., 2019. Aspects of the Archean-Proterozoic transition: how the great Huronian Glacial Event was initiated by rift-related uplift and terminated at the rift-drift transition during the break-up of Lauroscandia. Earth Sci. Rev. 190, 171–189. https://doi.org/10.1016/j.earscirev.2018.12.013.
Young, G.M., von Brunn, V., Gold, D.C.J., Minter, W.E.L., 1998. Earth's oldest reported glaciation: physical and chemical evidence from the Archean Mozaan Group (~2.9 Ga) of South Africa. J. Geol. 106 (5), 523–538. https://doi.org/10.1086/516039.
Zaharescu, D.G., Burghelea, C.I., Dontsova, K., Reinhard, C.T., Chorover, J., Lybrand, R., 2020. Biological weathering in the terrestrial system. In: Dontsova, K., Balogh-Brunstad, Z, Le Roux, G. (Eds.), Biogeochemical Cycles. American Geophysical Union, pp. 3–32. https://doi.org/10.1002/9781119413332.ch1.